SANDIA REPORT

SAND2003-3868
Unlimited Release
Printed November 2003

In-Situ Characterization of Colloidal Soft Solution Processes

Nelson S. Bell, David R. Tallant, and Mark Rodriquez.

Prepared by
Sandia National Laboratories
Albuquerque, New Mexico 87185 and Livermore, California 94550

Sandia is a multiprogram laboratory operated by Sandia Corporation,
a Lockheed Martin Company, for the United States Department of Energy's
National Nuclear Security Administration under Contract DE-AC04-94AL85000.

Issued by Sandia National Laboratories, operated for the United States Department of Energy by Sandia Corporation.

Available to DOE and DOE contractors from
U.S. Department of Energy
Office of Scientific and Technical Information
P.O. Box 62
Oak Ridge, TN 37831

Telephone: (865)576-8401
Facsimile: (865)576-5728
E-Mail: reports@adonis.osti.gov
Online ordering: http://www.doe.gov/bridge

Available to the public from
U.S. Department of Commerce
National Technical Information Service
5285 Port Royal Rd
Springfield, VA 22161

Telephone: (800)553-6847
Facsimile: (703)605-6900
E-Mail: orders@ntis.fedworld.gov
Online order: http://www.ntis.gov/help/ordermethods.asp?loc=7-4-0#online

SAND 2003-3868
Unlimited Release
Printed November 2003

In-Situ Characterization of Colloidal Soft Solution Processes

Nelson S. Bell, David R. Tallant, and Mark Rodriquez.
Chemical Synthesis and Nanomaterials
Sandia National Laboratories
P.O. Box 5800
Albuquerque, NM 87185-1411

Abstract

The purpose of this program was to investigate methods to characterize the colloidal stability of nanoparticles during the synthesis reaction, and to characterize their organization related to interparticle forces. Studies were attempted using Raman spectroscopy and ultrasonic attenuation to observe the nucleation and growth process with characterization of stability parameters such as the zeta potential. The application of the techniques available showed that the instrumentation requires high sensitivity to the concentration of the system. Optical routes can be complicated by the scattering effects of colloidal suspensions, but dilution can cause a lowering of signal that prevents collection of data. Acoustic methods require a significant particle concentration, preventing the observation of nucleation events. Studies on the dispersion of nanoparticles show that electrostatic routes are unsuccessful with molecular surfactants at high particle concentration due to electrostatic interaction collapse by counterions. The study of molecular surfactants show that steric lengths on the order of 2 nm are successful for dispersion of nanoparticle systems at high particle concentration, similar to dispersion with commercial polyelectrolyte surfactants.

Contents

Figures

Tables

Summary

The goals of this program were to explore experimental methods to measure kinetic effects between the colloidal stability of nanoparticles and their environmental conditions. This information will be useful to understanding the formation methods for nanoparticle materials, and their processing to create self assembled structures.

Attempts to observe the nucleation event of ZnO precipitation using Hexamethylenetetramine (HMT) by Raman spectroscopy were unsuccessful. The time necessary to measure zeta potential was also too long for the nucleation event to be resolved. Monitoring of zeta potential changes in a dispersion were possible.

The acoustic rheometer apparatus has been constructed. The development of the acoustic scattering models needed to infer particle size changes require further development, and studies using the instrument have not been completed. After development of the acoustic scattering algorithms, the instrument will be functional and provide assistance to studies of paste rheology and extrusion modeling.

Measurements of the flow of nanoparticles in microcapillaries under electrophoresis fields were not detectable for extrapolation of nanoparticle zeta potential by diffusion gradient methods. The use of fluorescent dyes was rejected as the method would not be comparable to studies of the kinetic effects of the desired system.

Experiments with dispersion of a model alumina nanopowder were successful in determining the best dispersant mechanism for achieving a high volume solid loading. Polyelectrolyte dispersants with minimum layer thickness were effective and showed the least sensitivity to excluded volume effects from the adsorbed layer thickness. Electrostatic repulsion is theorized to be ineffective due to the background salt concentration inherent to nanopowder surface area charging effects.

Studies with the alumina nanopowder found that steric dispersants with estimated thickness on the order of 2.5 nm were successful for achieving a high solids loading equivalent to that of a polyelectrolyte layer. Steric dispersants of lower thickness exhibited flocculated rheological response in relation to their thickness. Rheological fitting with conventional models were of limited effectiveness in understanding the data. It is proposed that dissolved gas from the atmosphere increases the adhesion forces between surfaces to cause the increased elastic character and low solids loading for fluid flow.

Success in the understanding of routes to stabilization of nanoparticles has been achieved. Resolution of the *in situ* interfacial processes in the formation of nanoparticle colloids could not be achieved in these studies.

Chapter 1. Characterization of Nanoparticle Nucleation

In the synthesis of nanosized particles, it is necessary to control the processes of nucleation, growth, and aggregation in order to fabricate a uniform dispersion. In the nucleation stage, ionic strength is usually elevated and traditional considerations of electrostatic stabilization would predict that colloidal stability is not possible unless the species on the surface are highly charged. Growth units are also generally considered to be polynuclear species, which can be multiply charged. The transitory character of these growth units and any surface modifiers will impact the development of a dispersion of uniform and unagglomerated particles.

The zeta potential of particles is the most common measure of their colloidal stability in aqueous fluids, and it is important in many non-aqueous fluids. Commercial instruments for the determination of zeta potential operate via either light scattering or electroacoustic methods to measure the electrophoretic mobility of particles. These instruments have sample cells that are titratable, chemically monitored, and thermally controlled. Particle size distributions are typically monitored only in the dilute and stable case by light scattering. These studies do not characterize the kinetic effects of adding a reactant at the surface or in solution. We explored the addition of an optical probe (Raman or IR) to investigate the presence of the growth species and particle size. The purpose of these studies is to reveal novel aspects of particle stabilization during synthesis in tandem with chemical information regarding the source components in the fluid.

The formation of zinc oxide using the decomposition of Hexamethylenetetramine (HMT) proceeds by a change in pH induced by the decomposition products of HMT from acidic to neutral solution pH. The reaction in solution is written as

$$Zn^{2+}(aq) + OH^{-}(aq) = ZnO(s) + H^{+}(aq)$$

The species behavior of Zn ions is given in Baes and Mesmer (1). In the acidic region, zinc ions hydrolyze as $ZnOH^{+}$ and Zn_2OH^{3+} before precipitation occurs in the neutral region. Precipitation at room temperature will form the hydroxide form, but at elevated temperature ZnO becomes stable. This system was chosen for study for the reasons of ease of processing under ambient laboratory conditions, the reaction proceeds in aqueous solvent, reaction at elevated temperature would preclude the influence of carbonate ions, and a number of studies using growth controlling agents and polymers are known (2-6).

The experimental procedure for precipitation of ZnO using HMT is as follows. A solution of $Zn(NO_3)_2 \bullet 6H_2O$ of 0.1 M concentration is prepared in deionized water. Dissolution requires the pH to be lowered by the addition of nitric acid (1.0 N) to give a solution pH of 5.5. Hexamethylenetetraamine (HMT) concentrations of varying strength (0.01 – 0.06 M) are formed in the Zinc nitrate solution by determination of the amount of HMT required for a sample volume and addition of the dry powder directly. PH is adjusted by the addition of nitric acid to 5.5, and the presence of the HMT acts as a significant buffer at room temperature. This solution is then filtered through a 0.2 micron pore size filter paper. After preparation, the solution is then heated to 90 ºC using either a mantle or an oil bath under magnetic stirring, and the reaction proceeds for periods of between 4 and 24 hours. The precipitate generally forms within 15 minutes of reaching 90 ºC. The solution pH is known to increase initially from 5.5 to approximately 7, then as the reaction proceeds, the pH can become slightly acidic and stabilize near 6.5.

Investigations for use of Raman spectra to follow the precipitation reaction of zinc oxide produced by Hexamethylenetetraamine (HMT) were performed with Dave Tallant. Raman spectra can be taken in a non-invasive manner to characterize the decomposition of the HMT, the formation of metastable chemical species in solution, and the formation of the desired zinc oxide phase. Initial measurements of the container, solution, and precipitate showed that the container would have to be modified in order to effectively collect signal of the ZnO without overlap of peaks. A calcium fluoride window was used with a glass vial to allow data collection, and the effects were sufficient. In studying the system, we found that the base-producing chemical hexamethylenetetraamine did not decompose as expected from survey of the literature. The reason for the stability of the HMT is unknown, and further examination of the literature is underway. A possibility is the formation of a zinc-HMT complex that stabilizes the HMT and reduces the supersaturation of the zinc in the solution; both effects are detrimental to the synthesis of the desired zinc oxide.

As a prelude to the in-situ measurements of the reaction mixture, we obtained Raman spectra of reactants, solvents and container materials (Figures 1 and 2). Figure 1 includes a Raman spectrum of zinc oxide powder, which we expected to have features similar to that of zinc species as they precipitate in solution. This figure also includes a

spectrum of a possible solvent, ethanol. Since ethanol has a potentially interfering Raman band near that of the most intense zinc oxide band, we decided instead to use water as a solvent. Water has only some broad, low-intensity, Raman features below 1000 cm^{-1}, and these are largely overwhelmed by broad Raman bands from the glass of the container used to hold the reaction mixture. The Raman bands in the "Water in glass vial" spectrum in Figure 1 are predominantly from the glass vial. Although it is possible to reduce the intensity of the glass bands by sampling the solution away from the glass/solution interface and to subtract the glass bands using reference spectra, they potentially interfere with our ability to detect Raman bands due to zinc oxide. For this reason we also experimented with a glass vial that had a calcium fluoride (CaF_2) window epoxied to it. By illuminating the reactant solution and collecting Raman-scattered light through the CaF_2 window, we prevent bands due to the glass vial from appearing in the spectra. CaF_2 has only a low frequency Raman band that does not overlap much of the Raman region of zinc oxide. However, the CaF_2 emits fluorescence from rare earth impurities. In order to suppress this fluorescence, we had to excite the Raman scatter with 488 nm light (if the CaF_2 window was used) rather than the 514 nm light used otherwise. The 488 nm wavelength has less power available and may not excite Raman scatter in zinc oxide as efficiently.

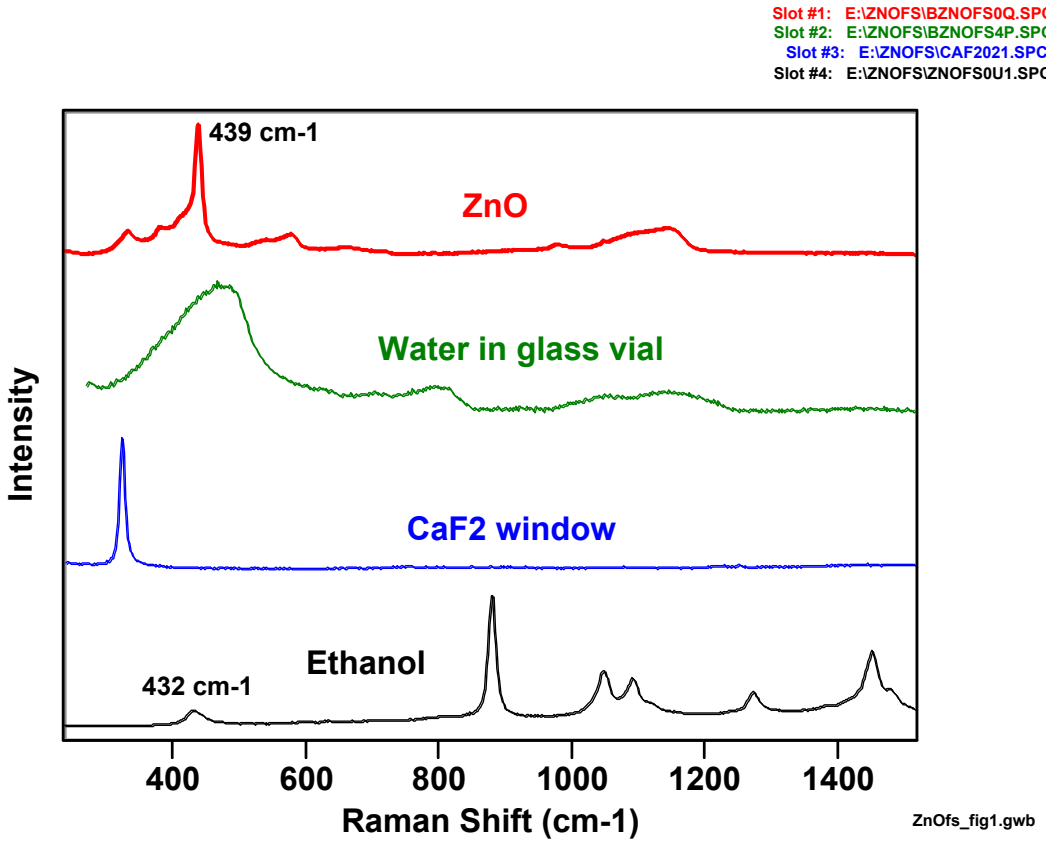

Figure 1 Raman spectra of some materials involved in chem. prep. of zinc oxide.

The reagents used to form zinc oxide include $Zn(NO_3)_2$ (19.5 mL of 0.25 – 0.35 molar in water solution), pH adjusted with nitric acid, to which 0.5 to 1 mL of 1 molar hexamethylene tetraamine (HTM) is added. At a solution temperature near 80°C, the HMT is supposed to decompose (on an time scale of minutes), and the ammonia formed on its decomposition should increase the pH of the solution from the 4 – 6 range to greater than 10, causing zinc to precipitate as zinc oxide/hydroxide species. Constant stirring of the solution keeps the zinc precipitate particles dispersed in solution, where they can be monitored by the Raman technique.

A major problem we encountered is that the pH never rose above the 4-6 range, and only a small fraction of the zinc oxide precipitated. When we monitored the HMT by itself in a heated solution for 40 minutes (see Figure 2), we found no evidence for decomposition of HMT. There were no new Raman bands, which would be evidence of decomposition products, and there was no decrease in the intensity of the HMT bands. Compared to the HMT spectra obtained at room temperature, some of the HMT bands actually increased slightly in intensity during

heating, probably because of differences in band shapes at elevated temperatures. Continued heating over several days likewise produced no evidence that HMT was decomposing. This stability of HMT at elevated temperatures is not understood, since literature reports indicate that it will decompose.

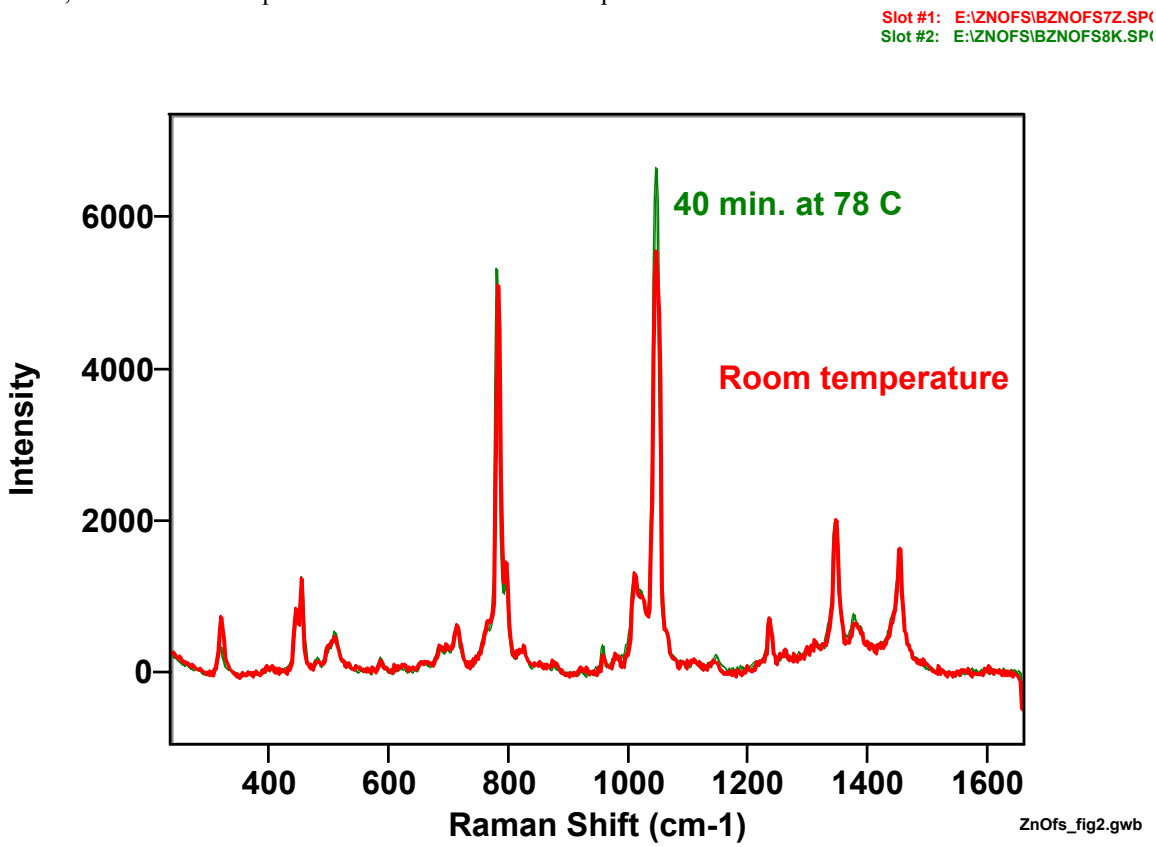

Figure 2 Raman spectra of 1M hexamethylene tetraamine (HMT) in water.

Despite the problems in getting the HMT to decompose, increase the pH and efficiently precipitate zinc oxide species, we attempted to monitor zinc nitrate solutions (they did turn slightly cloudy, indicating some precipitation) during heating with HMT. To a hot (77 - 79°C) solution of 19 mL of 0.35 M $Zn(NO_3)_2$ was added 1 mL of 1 M HMT, and Raman spectra were obtained in-situ for 30 minutes. This experiment was carried out in a glass vial and in a glass vial with an epoxied CaF_2 window. In the experiment carried out in the glass vial (no CaF_2 window), the pH decreased from 4.94 at the beginning of the experiment to 4.83 after 30 minutes. In order to remove solvent, reagent and container bands, we subtracted the Raman spectrum obtained at the beginning of the experiment from that obtained after 30 minutes at 76 – 80°C. Since the overall Raman intensity decreases as the solution becomes cloudy, we had to scale the initial spectrum (to the intensity of the nitrate band at 1048 cm^{-1}) before the subtraction was performed. Ideally, this subtraction procedure should leave only those Raman bands in the spectrum that are due to species formed during heating period. In reality a small residue (a few percent of the original intensity) of the nitrate and HMT bands remain (see Figure 3). Also in the "Glass vial" spectrum of Figure 3, the broad feature from 400 – 600 cm^{-1} may be a residue of a band from the glass container. However, the two narrower features at 439 and 485 cm^{-1} are not due to the container, the solvent or the reagents. They are believed to be due to forms of zinc oxide, probably ZnO and a hydroxylated form. The intensity of these two bands tended to increase with heating time and the initial concentrations of $Zn(NO_3)_2$ and HMT. In the experiment carried out using an epoxied CaF_2 window on the glass vial, no bands due to zinc oxide species were observed (Figure 3). However, in this experiment the pH was initially at 4.39 and rose to 4.60. We also used the 488 nm laser line for excitation, which may be less sensitive to zinc oxide species. The CaF_2 window was crazed by the solution, and either its solution species or something from the epoxy may have affected the reaction. Note, however, how effectively the subtraction technique removed reagent bands from the spectrum. The sole CaF_2 band does not interfere with observation of the region where Raman bands from zinc oxide species are expected to occur.

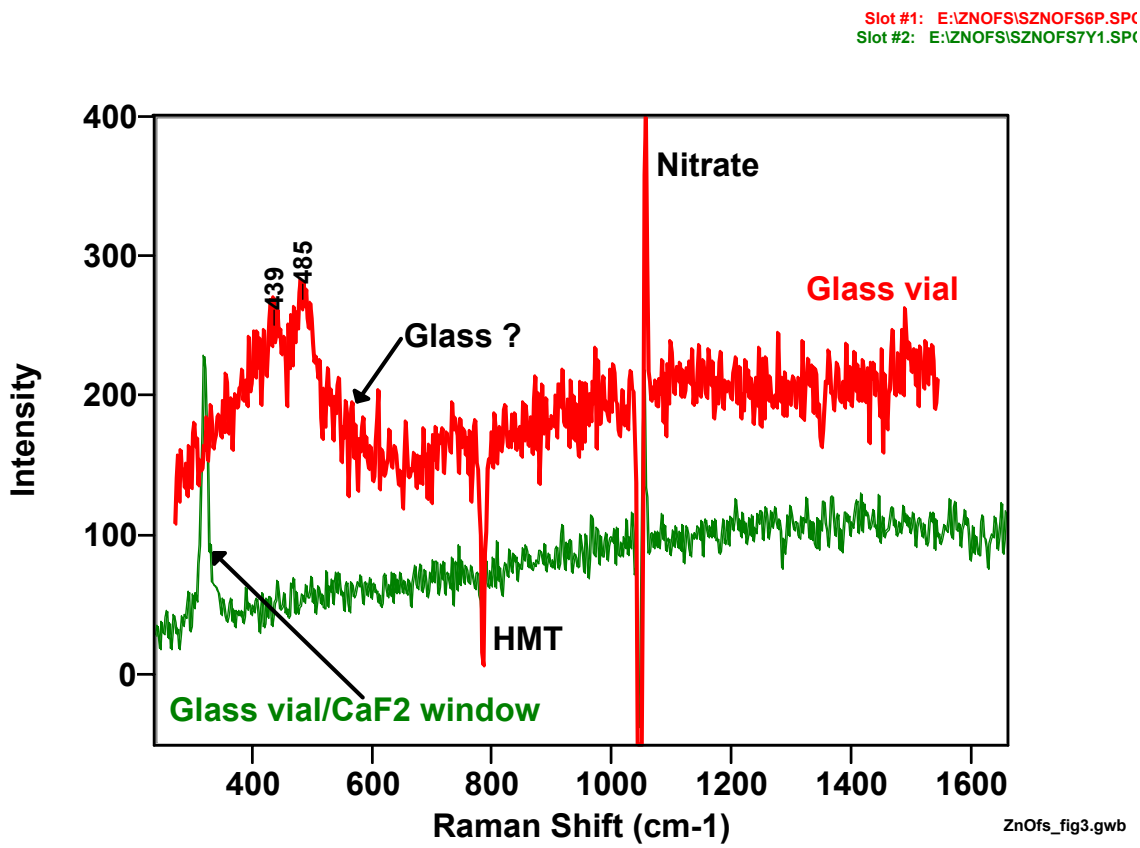

Figure 3 Raman Spectra of Zn(NO3)2 & HMT Reaction Mixture (80C, 30 min.). The data shown are the difference between spectra obtained after 30 minutes of heating and immediately after mixing the reactants.

We believe that we did observe Raman features from zinc oxide species precipitated in solution. The problem appears to be getting the majority of the zinc added as its nitrate to precipitate. We tried an experiment in which we added 0.35g (0.004 mole) of ZnO to 15 mL of a stirred water solution. The Raman intensity on the ZnO (439 cm^{-1}) Raman band, corrected to the same conditions as the spectra in Figure 3, was 500 intensity units. By comparison, the solutions whose spectra are shown in Figure 3 contained 0.0067 mole of zinc (0.35 M $Zn(NO_3)_2$ times 19 mL). If all of the zinc in these solutions had precipitated, the Raman signal from the resultant zinc oxide species should have peaked at hundreds of counts on the scale of Figure 3. Basically, it looks like the overall technique is feasible, if we can efficiently precipitate the zinc ions.

In Situ Measurement of Nanoparticles in a Reacting System

A study was performed using the acoustic spectrometer to attempt to measure the variation in zeta potential during the Stober precipitation reaction to form silica. The Stober reaction is performed in ethanol, with deionized water (9 M) and ammonium hydroxide (pH 12) as catalyst for the condensation of tetraethylorthosilicate (TEOS) to form monodisperse, spherical silica particles. For this measurement, silica particles must already be present, so silica nuclei were introduced by the addition of Ludox AS-40 to give a solids content of 1 volume %. This material is a suspension of silica particles that are uniformly 22 nm in size. Figure 4 shows the resulting zeta potential data vs. time.

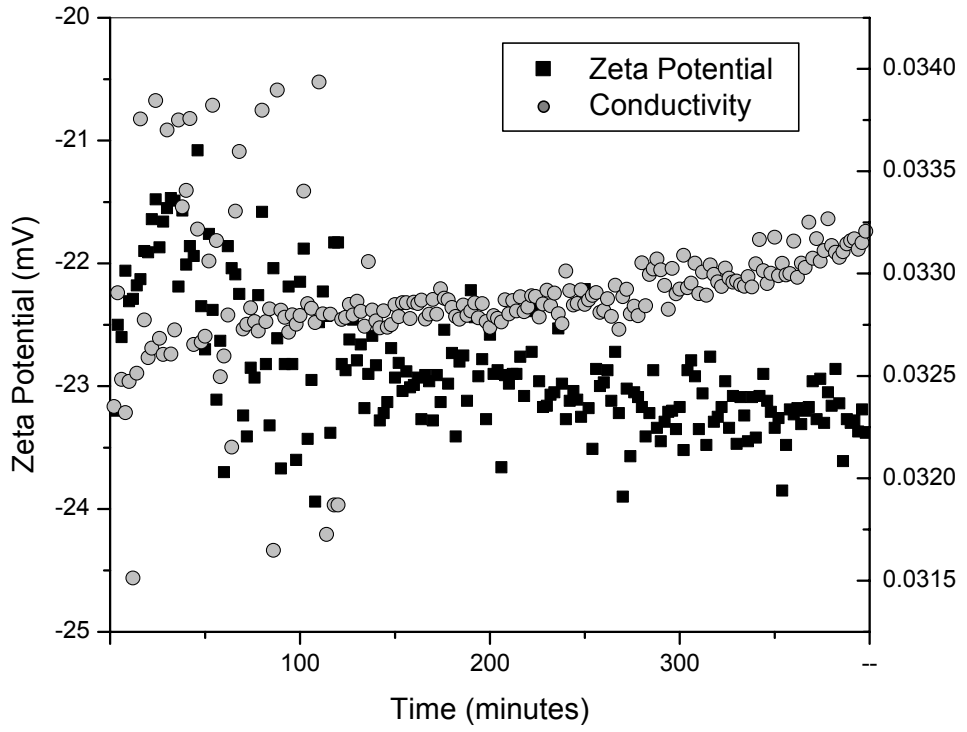

Figure 4 Zeta Potential vs. Time for Ludox AS-40 at 1 volume % in ethanol solvent during the reaction of TEOS in ammonium hydroxide.

The data shows a very minor decrease in the zeta potential value in the first hour, and corresponding scatter in the values of conductivity. As the reaction progresses, zeta potential increases slightly, as does conductivity. These observations show that the reaction species in this system do have a mild effect on the state of colloidal stability. As this is a well explored system known to successfully form monodisperse particles, it is not unexpected that large changes in the electrostatic potential are not seen. However, the data shows a general trend in the reaction to increase the conductivity (hence the salt concentration) and the state of the surface potential of the particles.

SUMMARY

The main conclusion of the study was that observation of precipitation is possible if the zinc ions can be made to precipitate efficiently. Direct observation of nanoparticle synthesis is a complicated problem. Optical methods such as UV-vis spectroscopy and Raman scattering appear to be viable, but ultrasonic characterization is limited to studies of interactions on formed nanoparticles. Our studies have shown that the process of nucleation requires a promoting agent and colloidal stabilizer, and the process of growth needs to be inhibited.

REFERENCES

1. C.F. Baes and R.E. Mesmer, The Hydrolysis of Cations, Krieger Publishing Co., Malabar FL, 1986.
2. A. Taubert, G. Glasser, and D. Palms, "Kinetics and Particle Formation Mechanism of Zinc Oxide Particles in Polymer-Controlled Precipitation from Aqueous Solution," *Langmuir*, **18** (2002) 4488-4494.
3. M. Oner, J. Norwig, W.H. Meyer, and G. Wagner, "Control of ZnO Crystallization by a PEO-b-PMAA Diblock Copolymer," *Chem. Mater.* **10** (1998) 460-463.
4. J.E. Rodriguez-Paez, A.C Caballero, M. Villegas, C. Moure, P. Duran, J.F. Fernandez, "Controlled precipitation methods: formation mechanism of ZnO nanoparticles," *J. Euro. Ceram. Soc.* **21** (2001) 925-930.
5. E.M Wong, P.G. Hoetrz, C.J. Liang, B.-M. Shi, G.J. Meyer, P.C. Searson, "Influence of Organic Capping Ligands on the Growth Kinetics of ZnO Nanoparticles," *Langmuir* **17** (2001) 8362-8367.

6. C.-H. Lu and C.-H. Yeh, “Influence of Hydrothermal Conditions on the Morphology and Particle Size of Zinc Oxide Powder,” *Cersm. Intl.* **26** (2000) 351-357.

Chapter 2. Development of Acoustic Rheometer

Macroscopic control of the flow behavior in the colloidal systems has generally focused on understanding the role of interparticle forces in suspension behavior and colloidal phase phenomena. Recently, the role of hydrodynamics in suspensions proves critical to understanding particle flow phenomena[1]. To evaluate these issues, a rheometer will be modified to measure the speed of sound of suspensions during flow. The speed of sound is influenced by the particle concentration and network structure, and exactly indicates the breakdown of particle structure by shear forces. These measurements would enable us to determine the formation of aggregated particles resulting from hydrodynamic forces. Developing this *Acoustic Rheometer* will involve modification of the sample cell of our existing rheometer with a transducer and associated signal processing equipment[2]. This instrument will allow for unique determination of gel points, structural transitions during flow, and shear induced particle aggregation.

Ultrasonic methods have been used for characterization of emulsions and food colloids, and density profiles of sedimenting particles, as well as the more advanced theory applied to fluid dispersions to determine particle size distribution and zeta potential (1-7). Application of acoustics to determine the structural transitions in suspensions due to hydrodynamic forces requires development of the acoustic cell and ultrasonic transducer needed to collect data, and the application of the proper acoustic model to interpret the data.

Figure 5 shows the hardware components used in the construction of the acoustic sensor modified cell. The cell is a reproduction of a standard cup and bob geometry for the rheometer. This was chosen to minimize efforts required to modify the existing rheometer equipment. The components include an ultrasonic transducer mounted perpendicular to the cup and bob wall. A pulse is generated by the signal generator, which travels through the cup wall, into the suspension, and is reflected from the bob back through the suspension to the cup wall, and finally to the transducer which acts as detector. A pulse-echo mode is established by the signal generator, and data is recorded as a series of pulses, which are separated by the time related to the speed of sound in the medium, and with diminishing intensity related to loss mechanisms in each material and at interfaces. Our cell is constructed of aluminum, and has a double wall construction to allow the cup to be thermally regulated by a water bath. The water also serves to couple the transducer signal to the inner cup interface. This interface is ground flat at the transducer interface to improve signal transfer. The transducer is a model V323, and the signal generator is an Epoch 4 instrument, both fabricated by Panametrics GE. The Epoch 4 is connected to a computer running ScanView Software to collect data automatically. Figure 6 shows a data collection result in ScanView of the transducer signal in a medium of deionized water. The first peak is the initial pulse, and the remaining peaks are reflections from the inner cup wall, cup-suspension wall, and the bob.

The raw data is used to determine the attenuation in the suspension by the ratio of the intensity of the peaks bracketing the signal.

$$\alpha = -\log\left(\frac{I}{I_0}\right) \tag{1}$$

The speed of sound in the suspension can be determined from the known distance between the inner cup wall and the bob (2 mm) and the time between the two reflection peaks. As this is a pulse-echo test, the distance traveled between the two reflections is twice the gap distance between the cup and bob.

$$V = \frac{2d}{t} \tag{2}$$

The scan view software collects this data automatically, as shown in Figure 6.

[1] R. Fitzgerald, "Hydrodynamics May Explain Like-Charge Colloidal Attraction," *Physics Today* **52** [2] (2001) p. 18-20.

[2] J.N. Coupland, Dept. of Food Science, The Pennsylvania State University.

Figure 5 Components to acoustic rheometer cell. These include ultrasonic transducer connected through the outer wall of the cooling jacket of the test cell, standard rheometer bob, and Epoch 4 (GE Panametrics) acoustic signal generator and receiver. The Epoch 4 is further connected to a computer running the Scan View software for data acquisition.

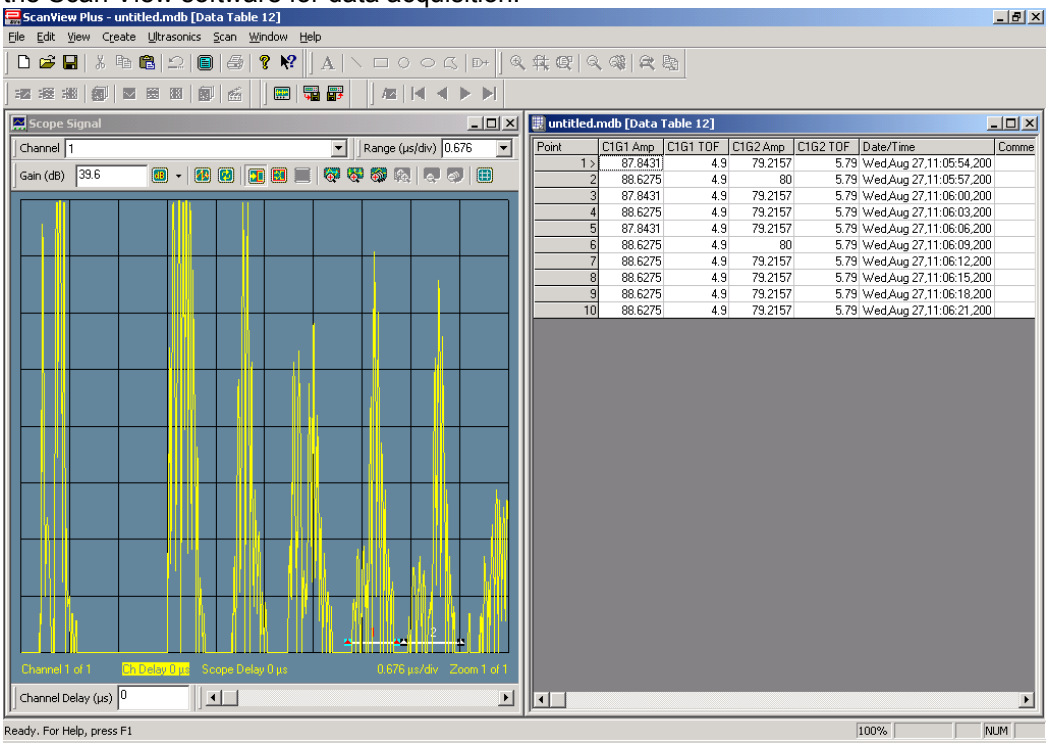

Figure 6 Acoustic response of a water filled cell and data acquisition by the Scan View Software program.

The determination of particle size by acoustic methods relies on the measurement of a range of frequencies (generally 1 - 200 MHz) to determine the frequency where attenuation is maximized. Common applications in emulsions and dispersions are used to determine stability against sedimentation or phase separation, using volume fraction profiles. In this application, the volume fraction will be assumed constant due to the shear forces in the measurement cell. The model employed must account for the variation in attenuation and phase speed with frequency related to the volume fraction of solids, phase densities, and phase sound velocity and compressibility.

There are six mechanisms for loss in a dispersion of one phase in another. These include (a) intrinsic losses, (b) viscous loss, (c) thermal loss, (d) scattering, (e) structural loss, and (f) electrokinetic loss. For systems where the solid phase has a significantly higher density than the fluid, the dominant losses are intrinsic, viscous, structural, and scattering. Viscous losses are generated by the shear wave generated by the particle oscillating in the acoustic field, due to the difference in density between the phases. Intrinsic losses result from the interaction of the sound wave with the materials analogously to absorption. Structural losses are created in structured systems, where the oscillation of the network of interparticle links causes loss.

Relation of the measured data to a model involves first the determination of the complex wave number of the system. For a liquid, this is given by $\left(\frac{k}{\omega}\right)^2 = \rho\kappa$ where k is the complex wave number given by $k = \omega/c + i\alpha$, with the angular frequency given by $\omega = 2\pi f$, with the parameters: f as the frequency, c is the ultrasonic velocity, α is the attenuation coefficient, κ is the adiabatic compressibility, and ρ is the density. In a two-phase system, the equations must be modified to relate the volume averaged values of the component phases. The ideal relationships for speed of sound, attenuation, compressibility, and density are as follows.

$$c_V = \frac{1}{\sqrt{\rho_V \kappa_V}} \tag{3}$$

$$\alpha_V = \phi\alpha_2 + (1-\phi)\alpha_1 \tag{4}$$

$$\kappa_V = \phi\kappa_2 + (1-\phi)\kappa_1 \tag{5}$$

$$\rho_V = \phi\rho_2 + (1-\phi)\rho_1 \tag{6}$$

The parameters are ϕ is volume fraction of the disperse phase, subscripts 1 and 2 refer to the fluid and disperse phases respectively, and V refers to the volume averaged quantities. The attenuation coefficient is generally larger than that predicted by equation 4, due to scattering effects. Models to account for these losses include physical models, and more recent coupled phase theories. It has been found that the general modeling of attenuation of colloidal dispersions must be solved numerically. A general relationship between particle size and the frequency of maximum attenuation is given by

$$ka = \frac{\pi d}{\lambda} \approx 2 \tag{7}$$

Models for the attenuation of sound by a disperse phase include physical models as given by Urick, or the modified Urick's model (10-12), Morse, Harker and Temple's model (13,14), Temkin's model (15) and scattering theory (16, 17). Additionally, there are coupled phase models that solve the attenuation problem more accurately using numerical methods (18-21). These routes using numerical approaches have been found to be more accurate and are required for the most accurate modeling of the data.

Alvarez-Arenas et al. performed studies similar to the design of the acoustic rheometer and modeled this with the physical models of Urick, Temkin, and Harker-Temple. Their results for the three models investigated showed that none were completely adequate for modeling attenuation and phase velocity in the resonant cell. Further theory development in the behavior of particle clusters was suggested as necessary for proper interpretation of the collected data.

For our application using ultrasonics to characterize yield stress, gel point, and structuring phenomena under shear conditions, it will be necessary to develop capability with a multiphase flow model for proper treatment of the data. Such development could be carried out in Org 9000, but was beyond the financial scope of this program. Development of the hardware to perform frequency scans is available and relatively inexpensive. It requires only the purchase of broadband transducers. The instrumentation is capable of performing a Fourier transform of the broadband pulse to deconvolute the frequency response of the system. With a proper numerical model, the modified instrument will be applicable to a number of particulate suspensions, and these studies will be initiated as the capability is further developed.

REFERENCES

1. T.K. Basaran, J.N. Coupland, and D.J. McClements, "Monitoring Molecular Diffusion of Sucrose in Xanthan Solutions using Ultrasonic Velocity Measurements," *J. Food Sci.* **64** (1999) 125-128.
2. R. Chanamai, J.N. Coupland, D. J. McClements, "Effect of Temperature on the Ultrasonic Properties of Oil-in-Water Emulsions," *Coll. Surf. A* **139** (1998) 241-250.
3. T.E Gomez Alvarez-Arenas, L.E. Segura, E.R.F. de Sarabia, "Characterization of Suspensions of Particles in Water by an Ultrasonic Resonant Cell," *Ultrasonics* **39** (2000) 715-727.
4. A.S. Dukhin and P. J. Goetz, "Characterization of Aggregation Phenomena by means of Acoustic and Electroacoustic Spectroscopy," *Coll. Surf. A* **144** (1998) 49-58.
5. S.B. Johnson, A.S. Russel and P.J. Scales, "Volume Fraction Effects in Shear Rheology and Electroacoustic Studies of Concentrated Alumina and Kaolin Suspensions," *Coll. Surf. A* **141** (1998) 119-130.
6. J.C. Austin and R.E. Challis, "The Detection of Structural Transformations in Kaolin Suspensions by Ultrasound," *J. Coll. Interface Sci.* **220** (1999) 6-12.
7. P.V. Nelson, M. J.W. Povey, and Y.Wang, "An Ultrasound Velocity and Attenuation Scanner for Viewing the Temporal Evolution of a Dispersed Phase in Fluids," *Rev. Sci. Instruments* **72** (2001) 4234-4141.
8. Ya. M. Zhileikin, Yu. I. Osipik, and N.I. Pushkina, "Diffracting Acoustic Beams of Finite Amplitude in Marine Sediments," *Acoust. Phys.* **49** (2003) 305-311.
9. A.S. Schaafsma and A.E. Hay, "Attenuation in Suspensions of Irregularly Shaped Sediment Particles: A two-parameter equivalent spherical scatterer model," *J. Acoust. Soc. Am.* **102** (1997) 1485-1502.
10. R.J. Urick, "A sound velocity method for determining the compressibility of finely divided substances," *J. Appl. Phys.* **18** (1947) 983-987.
11. R.J. Urick, "The absorption of sound in suspensions of irregular particles," *J. Acoust. Soc. Am.* **20** (1948) 283-289.
12. V.J. Pinfield, M.J.W. Povey and E. Dickenson, *Ultrasonics* **34** (1996) 695.
13. A.H. Harker, J.A.G. Temple, "Velocity and Attenuation of Ultrasound in Suspensions of Particles in Fluids," *J. Phys. D Appl. Phys.* **21** (1988) 1576-1588.
14. A.H. Harker, P. Schofield, B.P. Stimpson, R.G. Taylor, J.A.G. Temple, "Ultrasonic propagation in Slurries," *Ultrasonics* **29** (1991) 427-438.
15. S. Temkin, "Sound Propagation in Dilute Suspensions of Rigid Particles," *J. Acoust. Soc. Am.* **103** (1998) 838-849.
16. Y. Wang and M.J.W. Povey, *Colloids Surf. B* **12** (1999) 417
17. A.S. Schaafsma and A.E. Hay, "Attenuation in suspensions of irregularly shaped sediment particles: a two-parameter equivalent spherical scatterer model," J. Acoust. Soc. Am. **102** (3) (1997) 1485—1502.
18. W. Han and H.P. Pendse, "Unified Coupled Phase Continuum Model for Acoustic Attenuation in Concentrated Dispersions," in Handbook on Ultrasonic and Dielectric Characterization Techniques for Suspended Particulates, Ed.V.A.. Hackley and J. Texter, The American Ceramic Society, Westerville, OH, 1998, pp.129-152.
19. A.S. Dukhin, P.J. Goetz, and V. Hackley, "Modified log-normal particle size distribution in Acoustic Spectroscopy," *Coll. Surf. A* **138** (1998) 1-9.
20. A.S. Dukhin, V.N. Shilov, H. Ohshima, and P.J. Goetz, "Electroacoustic Phenomena in Concentrated Dispersions: New Theory and CVI Experiment," *Langmuir* **15** (1999) 6692-6706.
21. A.S. Dukhin, V. Shilov, and Y. Borkovskaya, "Dynamic Electrophoretic Mobility in Concentrated Dispersed Systems. Cell Model," *Langmuir* **15** (1999) 3452-3457.

Chapter 3. Dispersion Characterization of Nanoparticle Systems

INTRODUCTION

The goal of this aspect of the program was to determine the properties of nanoparticle dispersions that influence colloidal stability, self-assembly, and the achievement of high solid content slurries. The original proposal would apply confocal microscopy to the study of colloidal assembly. However, a confocal microscope was not available for study, and the cost of such an instrument was beyond the scope of the program. A second approach was attempted using microfluidic flow channels under an applied electric field to observe the electrphoretic diffusion of nanoparticles into a flow of solution without nanoparticles. Under the low pathlengths of the measurement cell, it was found that no signal could be detected by the CCD camera. One method considered to improve signal was to add fluorescent dyes to the system. However, this idea was discarded because if the dye and the surfactant or the surface interact, we would be changing the conditions of nanoparticle stability and invalidate the study. To meet the goal of the program, nanoparticles were examined using available instruments including the Haake RS300 rheometer and the DT 1200 acoustic spectrometer and electroacoustic zeta potential analyzer. A description of the attempts with the microfluidic cell will be given first, then the results of our study using a test nanopowder in the acoustic spectrometer and conventional rheometer.

Microfluidic Flowcell for the determination of Zeta Potential

In concept, the purpose of this cell was to introduce two streams of fluid into a cell, across which an electric field would be generated. For a stream containing stabilized nanoparticles mixing with a stream containing no nanoparticles, the concentration profile of the nanoparticles in solution will equilibrate based on Fick's laws of diffusion and the conditions for the hydrodynamic flow in the system. To this end, a simple cell was designed to introduce two flows of fluid between two gold electrodes, as shown in Figure 7. The cell has a depth of 5 microns, and a width of 100 microns. The gold electrodes on either side of the onset of the mixing regime are 500 microns long.

The diffusion profile of a microfluidic network of a (charged) nanoparticle solution and a pure solvent solution can be altered by applying an electric field. In this approach, rather than measure the value of an individual nanoparticle, the attempt was made to determine ensemble effects. A microscope equipped with wavelength filters was used to attempt to visualize the diffusion gradient as a nanoparticle stream and a solvent stream were mixed. The nanoparticles were not detectable under any magnification or optical filtering.

One option considered to improve the signal resolution is to utilize fluorescent tags on the nanoparticles. Studies of flow field dynamics are commonly imaged using fluorescent tagged particles (1-3). This requires that the nanoparticles are modified with the fluoroescent dye on the surface or interacting with the surface. Although effective for resolving fluid flow, the use of fluoroescent dyes to increase signal prevents measurement of pure systems. There are also concerns related to the effect of the electric field on the flow of the solvent. Flow modeling in an electric field is more complex not only from the mixing consideration, but also based on the resulting electro-viscous effects (4). Due to the many complications arising from the need to accurately model the flow field, including the effect of the electric field on the flow profile, and the need to fluorescently tag the nanoparticles, which will alter the state of the surface chemistry, this approach was terminated as a research avenue. Alternative methods were employed to evaluate the zeta potential of nanoparticles.

Routes for determining the zeta potential of nanoparticles can be performed under the restriction that a dispersion can be examined with a larger sample volume. There are reports in the literature in which dynamic light scattering procedures are used to collect zeta potential at elevated salt conditions, and the values at low electrolyte concentration are extrapolated (5). Another method applied streaming current measurements to a nanoparticle system to generate in situ measurements (6). A calibration curve using another system was employed to convert the current measured to a zeta potential. In this study, measurements were performed using the DT1200 acoustic spectrometer on a 1 volume % dispersion of a mixed oxide nanopowder supplied by TAL Materials. The material is a line compound of aluminum and titanium oxide. It was measured in deionized water, and titrated from pH 4 to pH 11, using ammonium hydroxide (1 N) as titrant. The resulting zeta potential profile as a function of pH is given in Figure 10, with conductivity of the solution during the measurement.

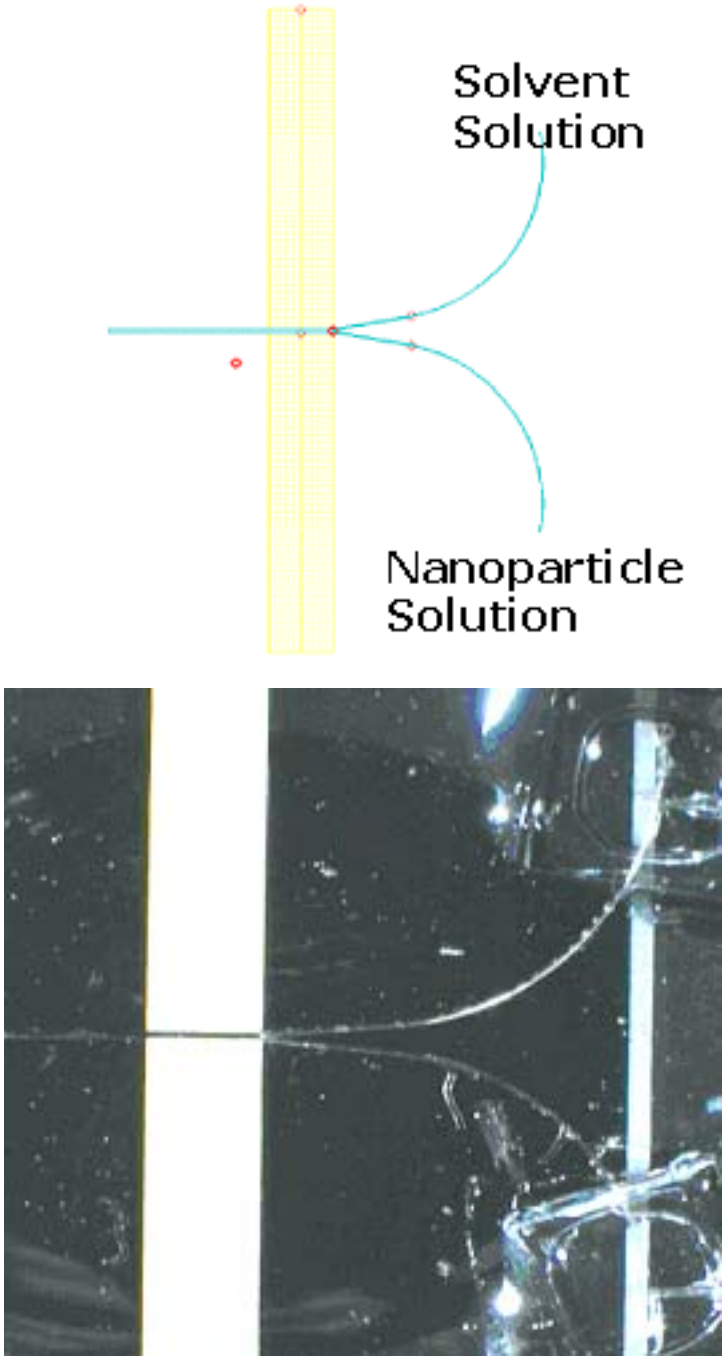

Figure 7 Schematic diagram and fabricated structure of the microfluidic flowcell for observation of nanoparticle electrophoretic diffusion.

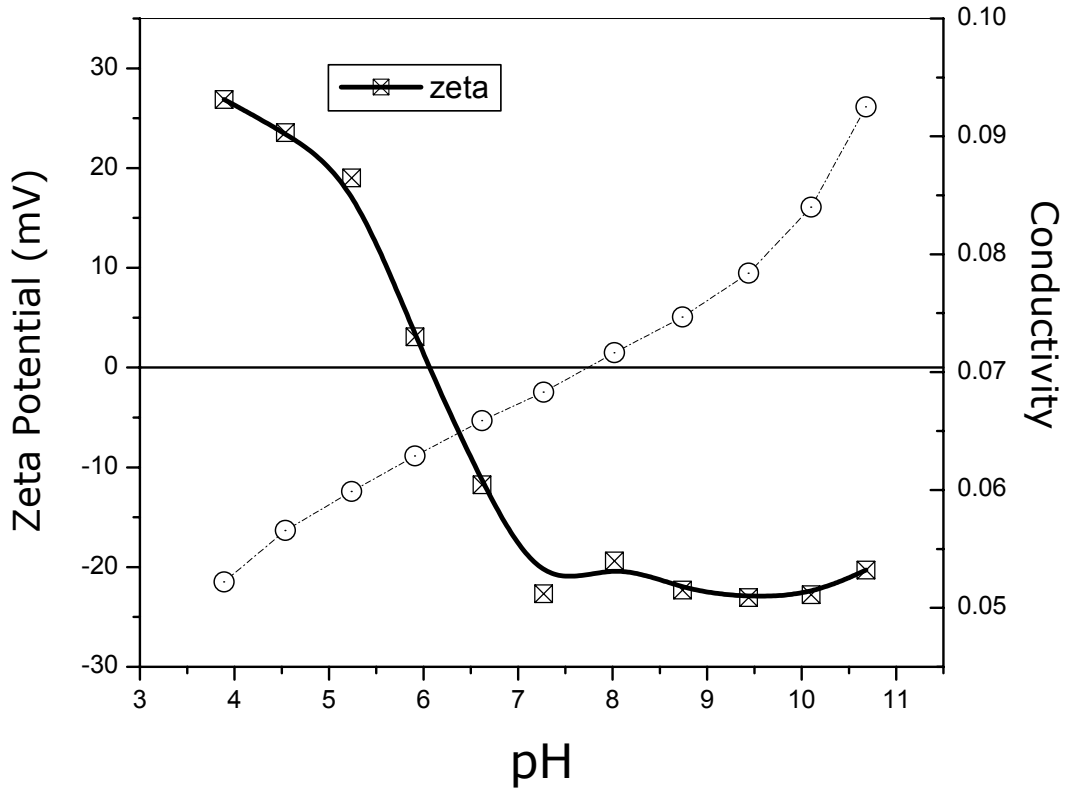

Figure 8 Zeta potential and conductivity values for TAL Materials $AlTiO_x$ compound nanopowder.

The particle size distribution measured by the instrument is also realistic, and indicates that this is a nanopowder. Figure 9 shows the acoustic spectra and particle size modeling of the instrument for the powder. The bimodal log-normal distribution shows that there is a significant component of the powder composed of particles near 35 nanometers in diameter, and a larger fraction in the submicron regime with a diameter of approximately 425 nm. This particle size distribution gives an excellent fit to the measured attenuation data. For a material with a known particle size distribution, it may be possible to perform kinetic studies of the effect of adding reactants, but this was not performed using this powder. Because the minimum concentration of particles to perform a measurement is 1 volume %, studies of the nucleation of nanoparticles cannot be performed in this instrument.

To conclude this section, it was possible to measure the zeta potential of nanoparticles in suspension for systems in which a large sample volume can be dispersed. The use of microchannels to determine the kinetic effects occurring during the precipitation or addition of reactants to a system was not feasible based on the low optical pathlength of a microchannel. The effect of the solution composition can be performed using larger dispersion volumes, but these techniques are not very applicable to rapid kinetic studies of the interface. Ultrasonic methods do not lend themselves to the observation of nucleation events. The measurements that have been performed can be used to study the dispersion of nanoparticles under conditions of elevated solids loading, and are presented in the following sections.

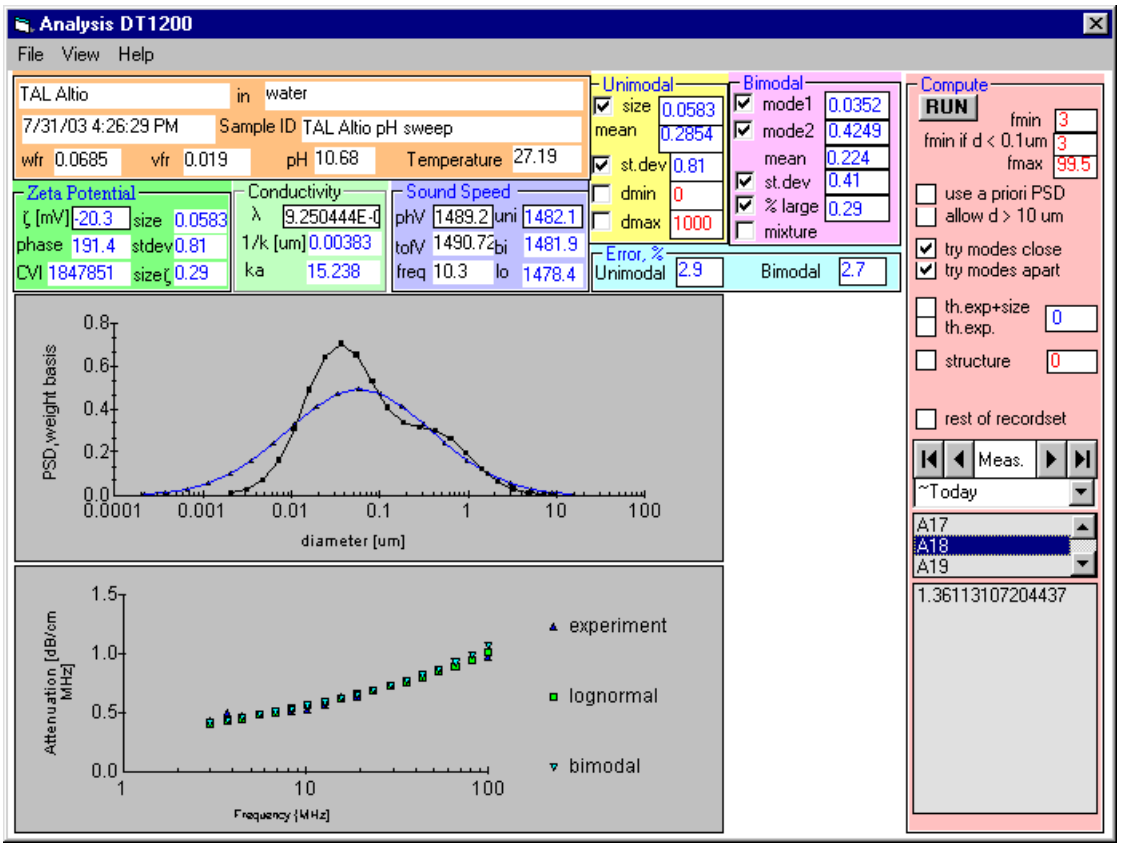

Figure 9 Acoustic spectra and particle size distribution fitting of aluminum-titanium mixed oxide nanopowder.

REFERENCES

1. R.B. Miles, A.P. Yalin, Z. Tang, S.H. Zaidi, and J. N. Forkey, "Flow field imaging through sharp-edged atomic and molecular 'notch' filters," *Meas. Sci. Technol.* **12** (2001) 442-451.
2. J.B. Edel, S.K. Hill, and A.J. de Mello, "Velocity measurement of particulate flow in microfluidic channels using single point confocal fluorescence detection," *Analyst* **126** (2001) 1953-1957.
3. P. Desevaux, D. Homescu, P.K. Panday, J.P. Prenel, "Interface measurement technique for liquid film flowing inside small grooves by laser induced flurorescence," *Appl. Therm. Eng.* **22** (2002) 521-534.
4. D. Li, "Electro-viscous effects on pressure-driven liquid flow in microchannels," *Coll. Surf. A* **195** (2001) 35-57.
5. H.S. Kang, S.-S. Kwon, Y.-S. Nam, S.-H. Han, and I.-S. Chang,, "Determination of Zeta Potentials of Polymeric Nanoparticles by the Conductivity Variation Method," *J. Coll. Interface Sci.* **255,** (2002) 352–355.
6. Wen-Cheng J. Wei,, Sheng-Chang Wang, and Fang-Yuan Ho "Electrokinetic Properties of Colloidal Zirconia Powders in Aqueous Suspension.," *J. Am. Ceram. Soc.,* **82** [12] (1999) 3385–92.

Chapter 4. Dispersion Characteristics of a Model Alumina Nanopowder

INTRODUCTION

Nanomaterials raise a number of possibilities for improvement of material properties. Examples where nanomaterial properties can be exploited include development of ultrafine grain size products, or nanostructured composites (1). In addition there are a number of examples where nanoparticles are used to lower the reaction temperature or conversion rate of bulk materials (2-4). The production of nanoparticles has great potential to impact processing science, but these materials raise a number of questions beyond traditional powder processing technology due to their small size. These questions include the formation of hard (i.e. sintered) aggregates during synthesis or processing, phase stability of the nanosized materials, variation in surface chemistry and dispersion forces between nanoparticles. When considering dispersion of nanoparticles, a robust dispersion mechanism is increasingly important, as the number concentration of a nanosized dispersion is much higher than with conventional powders, and the frequency of potential aggregation events is increased.

With conventional powder processing methods, the achievement of maximum solids loading in a suspension directly relates to improvements in final performance by reducing flaw size and concentration, increasing grain size uniformity, reducing shrinkage, stress and other benefits. The solids loading of conventional powders can be as high as 60 volume % or greater for the proper mixtures of particle sizes. In these systems, the length of the interaction used to stabilize the suspension is nearly negligible compared to the particle diameters, however with nanoparticles, the same stabilizing interactions are a significant fraction of the particle diameter and begin to have a deleterious effect on the achievable solids content of a fluid dispersion. These effects are generally related by the following equation for monosized particles.

$$\phi_{eff} = \phi\left(1+\frac{\delta}{r}\right)^3 \quad (1)$$

Here δ is the thickness of the dispersant interaction length, and r is the radius of the particle. The effective packing fraction ϕ_{eff} is often taken as that of randomly packed uniform spheres (0.63) but can vary based on particle size distribution, and ϕ is the true volume fraction of the powder. The effective volume fraction is always higher than the true volume fraction. This relationship sets a boundary for discussion of what constitutes a nanosized powder. From colloidal probe measurements of a number of typical commercial surfactants, the separation distances generated are on the order of 5-15 nanometers (5-8). Figure 10 shows that for particle sizes below 100 nm, the separation distance generated by the dispersant begins to affect the maximum attainable solids loading. The severity of the phenomenon increases as the particle size is lowered and as the steric length increases. A previous study in 6 nm titania suspensions stated that only polyacrylamide of molecular weight near 100,000 was sufficient to stabilize the particles against aggregation by providing a steric layer thickness of 6 nm (9). This steric length equals the particle diameter and limits the applications of these kinds of nanoparticle dispersions.

Dispersant molecules can be characterized by the forces they generate which counter the attractive van der Waals interaction. Small molecule dispersants are low molecular weight additives that specifically adsorb to the surface and often generate a strong surface charge. Lipids fall into this category, as well as multicharged acids that chemically complex with the surface. Their small size generally prevents the formation of a significant steric barrier to agglomeration, so their stabilization mechanism is largely electrostatic. Electrostatic stabilization is also possible on the native particle surface under the proper conditions of pH if there are enough ionizable surface groups. Electrostatic methods will be increasingly defeated at high salt concentrations due to screening effects and counterion condensation at the interface. Steric stabilization is generated by the adsorption of uncharged polymers which have extended loops and tails of the polymer. When particles are in close proximity, there are entropic and osmotic repulsions generated between the particle surfaces. Polyelectrolytes are also commonly used as dispersants that combine both the electrostatic repulsion as well as steric interactions between surfaces. Polyelectrolytes have been reported to act as efficient dispersants for 20 nanometer ceria particles (10).

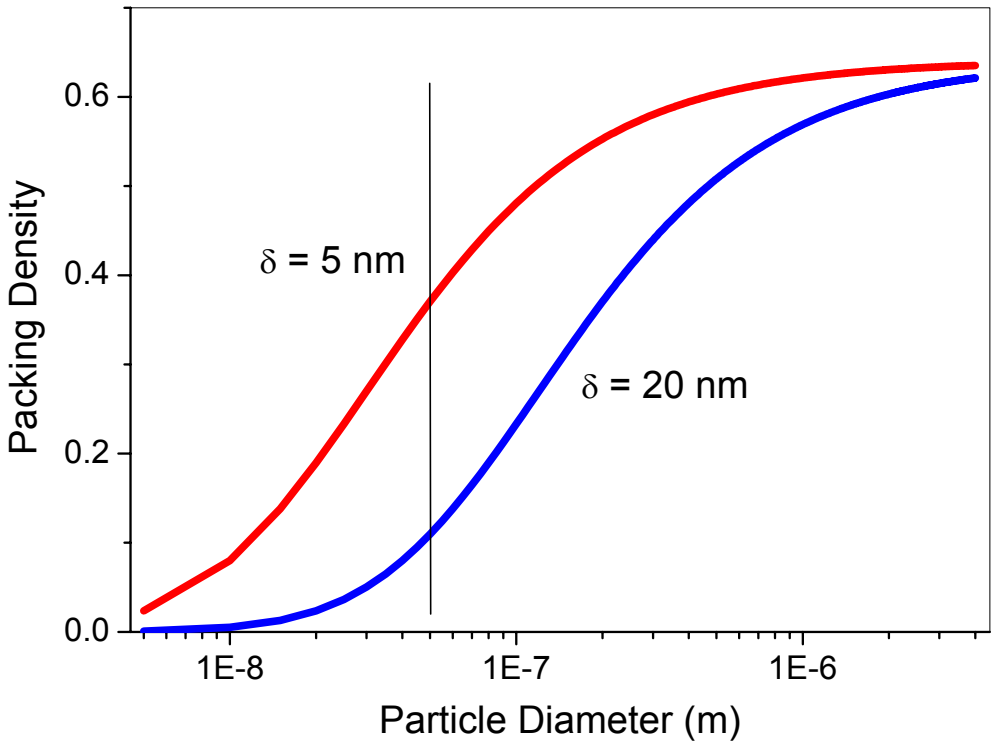

Figure 10 True solids loading curves for nanopowder suspensions with particle steric barriers of 5 and 20 nm. The maximum packing fraction is taken to be the same as random monodisperse sphere packing. The vertical line indicates the disparity between true volume fractions for a 50 nm diameter particle suspension.

In this study, the impact of these three classes of dispersants was studied on a newly available nanosized alumina powder. The powder was characterized for its morphology, phase stability, and dispersability. The rheology of the powder was examined in its native state as well as with a small molecule electrostatic dispersant, a linear polyelectrolyte, and a nonaqueous, steric copolymer. Both the rheological profile versus shear rate and the rise in viscosity with solids loading were examined to describe the effectiveness and processing range of these dispersants. Conclusions are drawn regarding the potential for using nanoparticle materials in conventional processing methods and in the type of molecules needed to promote the most effective dispersion of nanosized powders.

EXPERIMENTAL

The alumina powder was generously donated by TAL Materials. It is produced by liquid-feed flame spray pyrolysis (LF-FSP) of metalloorganic $[N(CH_2CH_2O)_3N]$ alumatrane by a vapor phase condensation method (11). It is composed of a mixture of transition alumina phases; primarily δ. The density of the powder was measured using a helium pyncnometer and found to be 3.5 g/cm^3.

The powder surface area was measured using an Accelerated Surface Area and Porosimetry System (ASAP) 2010 by Micromeritics. The sample was degassed at 350 °C for 12 hours to remove adsorbed water and CO_2. The surface area is 42.20 ± 0.07 (m^2/g).Transmission electron microscopy was performed on the as received powder dried on a carbon grid from aqueous suspension. The TEM was a Phillips CM30 operating at 300 kV.

XRD was performed using a Siemens D500 powder diffractometer equipped with a Cu sealed tube source and a diffracted beam graphite monochromator. A 1^o silt size was used for divergence, scatter, and receiving slits. Diffraction scans were collected from 10-80^o 2θ using a step-size of 0.05^o and a four second count-time. The powder phase stability when in aqueous suspension was studied by aging in aqueous suspension at pH 9 and characterizing the recovered powder.

Characterization of the particle size distribution in suspension and zeta potential was performed using an DT 1200 acoustic spectrometer[3]. The operational details of the instrument are described in ref. 12,13. Samples were prepared at 1 volume % in water, and dispersed using an ultrasonic horn programmed to emit 15 W in one second intervals for a duration of six minutes. Dispersant additions for the aqueous samples were made before sonication, and any pH adjustment was performed after sonication.

Rheological measurements were performed on a Haake RS300 rheometer using a cone and plate configuration with 1° cone angle and 60 mm diameter. The plate temperature was maintained at 25 °C by a recirculating fluid pump. Rheological characterization was performed using a 120 second preshear at 400 sec^{-1}, one minute of no motion, followed by a shear rate ramp from 0.1 to 400 sec^{-1} over 120 seconds, hold at 400 sec^{-1} for 30 seconds, and then decrease shear rate back to 0.1 sec^{-1} over 120 seconds. Samples for testing were made by adding dispersants to solvent in the proper proportion to form a 30 volume % suspension, and powder was added and mixed using an ultrasonic horn as needed to generate a fluid dispersion. For suspensions that did not flow under gravity, an ultrasonic bath was used to remove air bubbles from the suspension and prepare samples for rheological characterization. Successive measurement in the rheometer was performed by diluting the sample with pure solvent and remixing using the US horn for the initial samples, and the ultrasonic bath once viscosity became low and the sample exhibited fluid behavior. For the determination of relative viscosity, the solvent viscosity of α-terpineol was measured from 200 to 2000 sec^{-1}, and gave an average value of 29.48 mPas.

RESULTS

Figure 11 shows the powder morphology via transmission electron microscopy. The micrographs indicate that the powder is composed of primarily spherical or equiaxed particles that appear to be single crystals. The variance in particle size is between approximately 10 nanometers and 400 nanometers. The sizes of the particles show some outlying sizes greater than 100 nm, but indicate a majority of particles under 100 nm. Most striking about this powder is the absence of any discernable agglomerates. A number of micrographs were examined, and no agglomerates were visible in any of the photos. This result is remarkable in that hard (i.e. sintered) agglomeration is typical of a number of nanopowders produced via vapor phase decomposition. Hard agglomerate formation is often a critical concern in forming a dispersion of low viscosity.

Figure 12 shows the x-ray diffraction data taken from the native powder as well as following weeks of aging at pH 9. The as-received sample showed the presence of at least three phases: θ-alumina (PDF 86-1410), δ(tet)-alumina (PDF 46-1131), and δ(ort)-alumina PDF (46-1215). It does not indicate any of the gamma phase identified in powders described in prior publications (11). For the aged samples, an additional minor phase of Bayerite (PDF 83-2256) was also observed as indicated by the asterisks in Figure 3 (inset). Using the diffraction data in the 18-22^o 2θ range, it was possible to estimate the phase fraction of Bayerite. By using reference-intensity-ratios (RIR's)(14) from the PDF cards, the quantified data from the prior publication (11), and assuming the peak at ~19.5^o 2θ is due entirely to the θ-alumina phase, phase fractions for the Bayerite were determined to be approximately 1-2 wt% for the three aged samples.

Figure 13 presents the zeta potential data collected on the native powder, powder dispersed with Darvan C, and several dispersions with varying levels of citric acid additions. The isoelectric point can be adjusted using citric acid quite easily. The concentration of Darvan C used in this pH titration was chosen by monitoring the zeta potential of the native powder at pH 9 as the dispersant was titrated into the suspension, and surface coverage was assumed complete when the zeta potential remained constant against additional titration (not shown). The isoelectric point for this concentration of Darvan C is approximately 6, and produced the highest values of zeta potential at pH 9, where both citric acid and the Darvan C dispersant are expected to be fully deprotonated and generating the maximum negative zeta potential. The zeta potential values had a magnitude of less than -40 mV for any dispersant addition or pH condition.

[3] Dispersion Technology, 3 Hillside Ave., Mount Kisko, NY, 10579. www.dispersion.com.

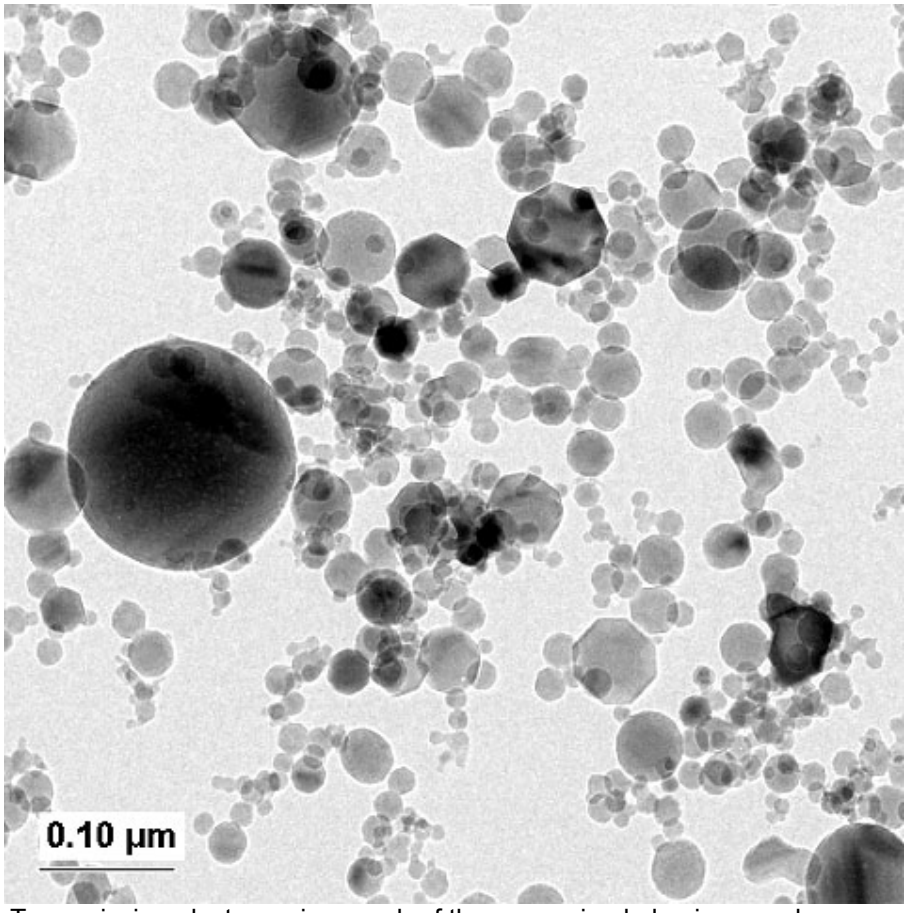

Figure 11 Transmission electron micrograph of the as received alumina powder.

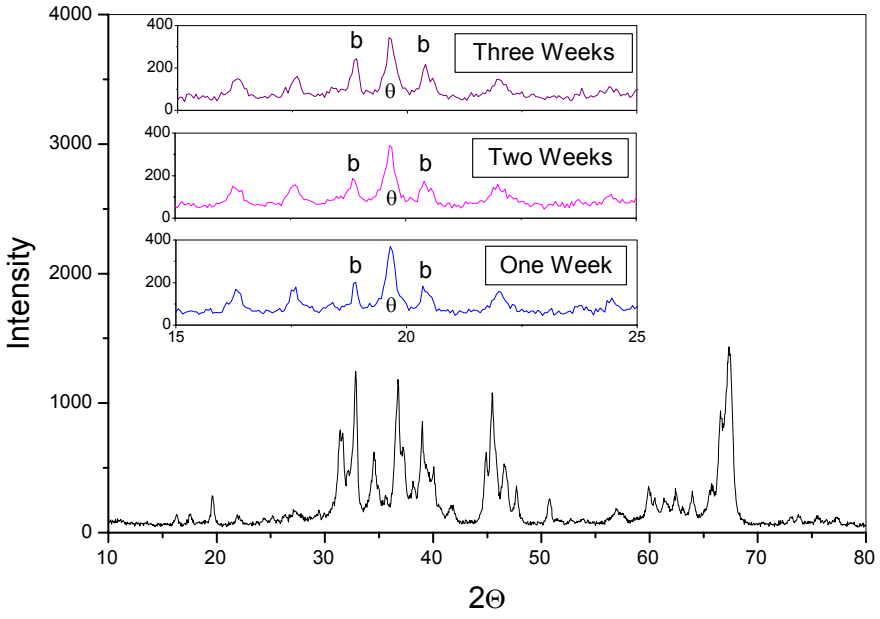

Figure 12 Phase composition of the powder as a function of aging time in aqueous suspension. The inset figures show the increase in bayerite peaks after aging at pH 9.

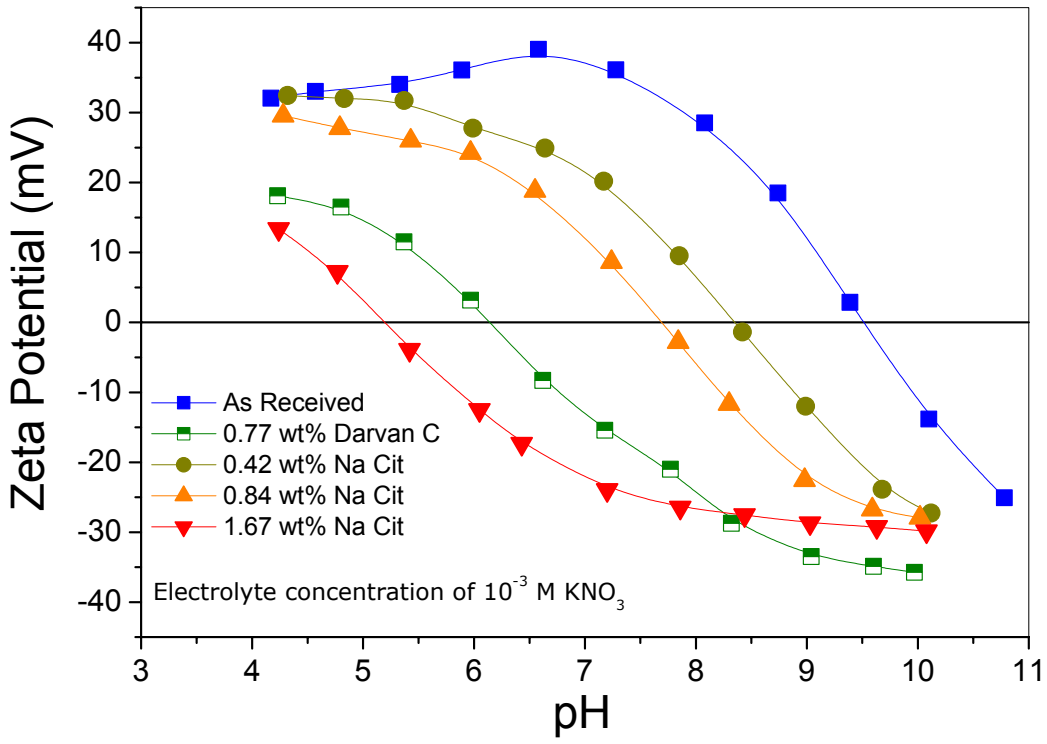

Figure 13 Zeta potential characterization of the powder as received, with Darvan C dispersant, and varying concentrations of citric acid.

Figure 14 shows the acoustic spectra of the native powder as measured for each pH during the titration from pH 4 to pH 11. These scans show excellent uniformity of the data points at frequencies greater than 20 MHz, but at lower frequencies, there is a progressive increase in attenuation as pH increases until a rough equilibrium is established above pH 6.58. Table 1 presents the particle distribution estimates determined from the acoustic spectroscopy data during the titration using data between 8 and 100 MHz, and indicates that the mean particle size begins to increase near pH 6.58. The % Error column refers to the error between the measured data and the calculated values of the attenuation spectra. The structure factor characterizes particle association without aggregation and it is described further in the Discussion section. The inclusion of data points below 8 MHz created very high values for error, and the zeta potential values calculated for the system differed by less than 2 mV by exclusion of the low frequency data. The change in attenuation spectra and development of aggregates correlate for a number of systems (12).

Figure 15 shows the rheology characterization determined for each dispersant near a solids loading of 30 volume %. The rheology of the Darvan C dispersed suspension at approximately 37 volume % is also presented to show the profile near its maximum in solids loading. The native powder was characterized at pH 5.4, the sodium citrate and Darvan C additions were both performed at pH 9, and the Hypermer KD1 as added in α-terpineol solvent. The added amount of Darvan C was found qualitatively to be higher than that determined from zeta potential measurements. The value chosen for rheology characterization was determined via measurements of viscosity at 15 volume percent solids as a function of added dispersant. Figure 7 compares the reduced viscosity of each dispersant versus volume fraction and the fit of the modified Krieger-Doughtery equation, given in Table 2.

Table 1 Fitting parameters and particle size predictions of the native TAL alumina powder in 10^{-3} M KNO_3 solution versus pH titration.

pH	Zeta Potential	Structure Factor	Mean Size (nm)	Standard Deviation (nm)	% Error
4.17	32.07	0.9	52.7	497	2.3
4.57	33.03	0.9	53.9	590	2.9
5.33	34.03	0.9	54.6	572	2.7
5.89	36.09	1.0	56.3	657	1.3
6.58	39.06	1.1	80.7	870	1.5
7.28	36.12	1.0	111	860	4.1
8.08	28.54	0.1	411	830	3.7
8.74	18.5	0.2	687	690	7.1
9.39	2.87	0.1	564	890	7.0
10.1	-13.82	0.1	615	780	6.4
10.78	-25.07	0.1	543	680	6.7

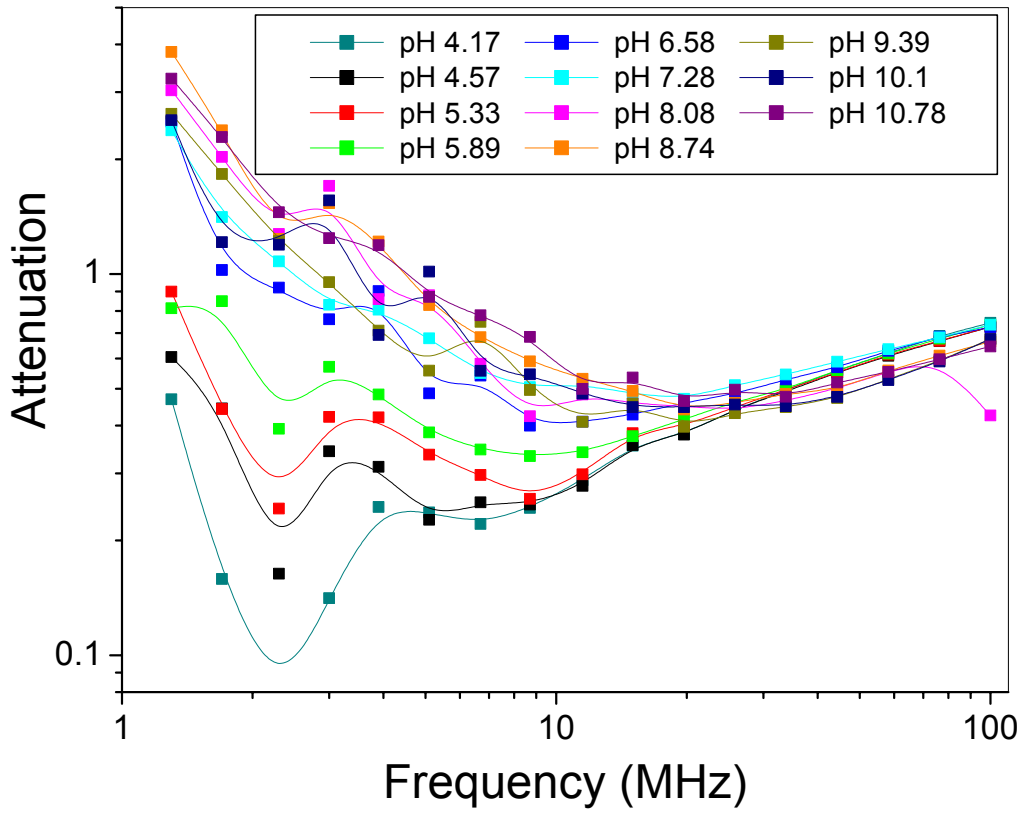

Figure 14 Acoustic attenuation spectra vs. Frequency for the as received TAL alumina powder as a function of pH.

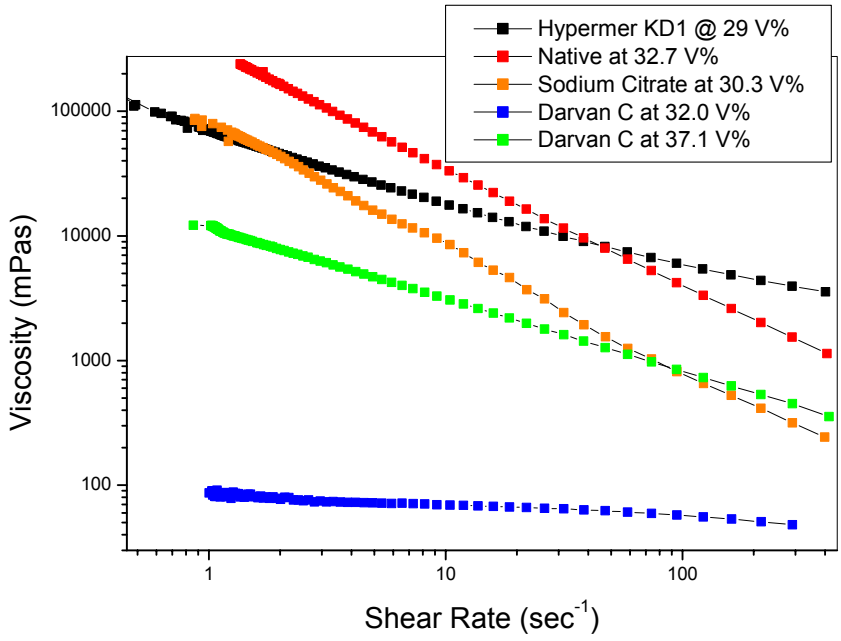

Figure 15 Rheological comparison of the TAL alumina powder dispersed with each dispersant near the solids content of 30 volume %. The Darvan C dispersed sample is also presented at 37.1 volume % to show its behavior at similar viscosity to the other samples.

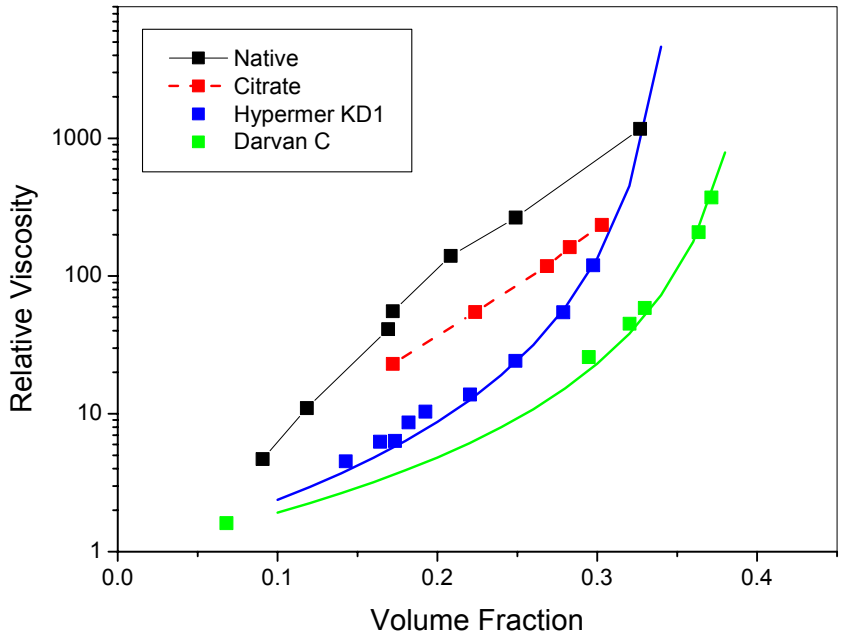

Figure 16 Relative Viscosity versus volume fraction for each dispersant at optimum concentration at a shear rate of 400 sec^{-1}. Lines are drawn to guide the eye for the Native and Sodium Citrate dispersed powders. The solid lines for the Hypermer KD1 and Darvan C dispersions are the Krieger-Doughtery equation fits with parameters given in Table 2.

Table 2 Krieger-Doughtery function parameters for dispersed suspensions.

Dispersant	Maximum Packing Fraction, ϕ_{max}	Viscosity Exponent, n
Darvan C	40.17 %	5.69
Hypermer KD-1	35.39 %	7.36

DISCUSSION

The equilibrium phase of alumina at room temperature and pressure is gibbsite, but bayerite is also stable. In processing these powders, it is possible to observe a phase transformation of the surface to an alumina hydroxide chemistry (15). In addition, nanopowders are known to be more soluble than conventional powders due to their high surface curvature as related by the Ostwald-Freundlich equation.

$$S_r = S_0 \exp\left[\frac{2\gamma_{sl}V_m}{RTr}\right] \tag{2}$$

Here S_0 is the solubility of a flat surface, V_m is the molar volume of the material, γ_{sl} is the interfacial free energy, R is the gas constant, T is absolute temperature, and r is the radius of the particle. The potential for increased solubility or variation in phase have been shown to affect future processing of nanopowders by Kwon and Messing (16), where the formation of hard agglomerates relates to the dissolution and reprecipitation of solute at particle contacts during drying. In Figure 11, the phase stability of the powder is indicated to be slightly unstable with respect to the formation of a small amount of bayerite phase. As the crystalline phase was detected, it is unlikely that a purely surface phase reaction has occurred in the powder. More likely, the smallest particles have undergone either dissolution and reprecipitation, or an *in situ* phase transformation to bayerite. Bayerite is typically produced by the slow carbonation of sodium aluminate solutions at 30 to 35 °C, but there are a number of methods based on the reaction of an aluminum source with water as long as the source is of very fine size (15,17). The solution pH for the aging study was pH 9, where the transition from the neutral $Al(OH)_3(aq)$ ion to the $Al(OH)_4^-$ anion is occurring. It is likely that at more alkaline pH the formation of an aluminum hydroxide precipitate will be promoted by the increased dissolution rate of the smallest nanoparticles. For this study, the bayerite quantity is not very significant, and the overall phase stability of the powder can be considered to be quite good.

The dispersion of conventional powders and their rheological properties relate rather closely to the calculated profiles of the DLVO theory (8). All identical materials exhibit an attractive interaction due to dipole interactions between molecules, which are collectively considered as van der Waals forces and characterized by the material Hamaker constant (18). As determined by the X-ray diffraction measurements, this powder is a mixture of phases that should be expected to have slightly differing van der Waals interactions. The particle size also impacts the strength of the interaction and thereby its interparticle stability range. For steric surfactants, either theories of the compression of adsorbed polymer layers are used to counteract the attractive van der Waals interaction, or a hard separation distance is chosen based on a estimate of the adsorbed layer thickness (19). In the case of electrostatic repulsion, the value of the zeta potential is often chosen as the surface potential for calculations of interparticle forces. These forces are also impacted by the solution electrolyte concentration, known to reduce the range of repulsion as ionic strength increases. Rowlands et al. showed that at extremely high salt concentrations (3 Molar) the background cations adsorb on the surface of the particles to affect their zeta potential (20).

When considering the dispersion of nanoparticles, a number of factors change in the typical consideration of the optimum method for dispersion. The powder surface area is increased and thereby the demand for a dispersant increases. In addition, the effects of curvature on the adsorbed amount and the interaction energy between particles are relatively unknown. For ionic dispersants, the higher dispersant concentration will introduce elevated concentrations of background electrolyte and collapse the repulsive forces between particles especially as the solids loading is maximized. Predictions of the interactions between nanoparticles by Kallay and Zalac suggest that electrostatic repulsion will fail for nanoparticles and that nanoparticles will aggregate more rapidly than micron-sized particles due to their higher number concentration (21)

In this study, it was desired to compare the effectiveness of conventional surfactants in the dispersion of a powder where the main particle size is small enough that the interaction length of the stabilizing interaction significantly impacts the maximum solids loading achievable in the system as well as the rheological characteristics. For that reason, the evaluated surfactants were chosen as a small molecule surfactant that is expected to have an extremely small steric component, a linear polyelectrolyte and a purely steric polymer. In this study, the differences

in molecular weight that affect polymer interactions were not able to be characterized, but the products used are all commercially available and have a history of use in industrial processes.

The stability of a suspension can be evaluated from the acoustic attenuation spectra taken by our instrument and presented in Figure 14. Under acidic pH, the acoustic attenuation spectra versus frequency provides low adsorption that is similar to published values for the nanosized Ludox standard used to calibrate the instrument (12). Table 1 presents the particle size distribution data for the native powder as a function of the pH titration. Aggregation occurs at and above pH 6.58 as shown by the increase in the mean particle size.

There are six loss mechanisms in acoustic spectroscopy (1)viscous losses (2) thermal losses (3) scattering losses (4) intrinsic losses (5) electrokinetic losses and (6) structural losses. Usually only the first four are treated, but structural losses can be significant. For dense rigid submicron particles in 1 MHz to 100 MHz frequencies, the viscous losses are dominant. They occur due to the shear wave generated by the particle oscillating in the acoustic pressure field. However, the theoretical treatment used by the instrument has another fitting component called the structure factor. The structure factor is a fitting parameter treating those losses in the system that relate to the forces between particles. The theoretical treatment models these forces as flexible "strings" connecting particles. This factor is initially large in the region of nanoparticle stability, and decreases to a small value during the aggregation process. The acoustic data indicates that in the region of nanoparticle stability, there are forces between the particles that cause their association. Velegol et al. have shown that in systems where the particle zeta potential is non-uniform, tangential forces can be developed between particles that cause a nontouching association (22). For this multiphase alumina powder, it is possible that the slight variations in van der Waals attraction and surface potential between the various phases and sizes are forming these non-touching particle associations. Once aggregation has occurred, these forces are no longer present between the large particle aggregates formed in the system. The process is more interesting in that this structure factor parameter actually appears to attain a maximum immediately prior to the system instability. Considering the balance of attractive van der Waals and stabilizing electrostatic forces in the system, the loss of strength of the stabilizing force as surface charge decreases would lead to a deeper secondary minimum in the interaction profile between particles until aggregation events are strong enough to lead to irreversible aggregation in the primary minimum. The prior work testing the use of the structure factor suggested that it would become significant under conditions of high solids loading approaching 40 volume % (12). Its additional insight to these nanoparticle suspensions is a surprising result.

Previously, citric acid (and its variant salts) and other molecular dispersants were studied for several alumina powders (23-28). The citrate ion adsorbs to alumina surfaces by a ligand exchange process to form surface groups. Two of the three carboxylic acid groups and the hydroxyl group interact as part of the surface complex, and the third carboxylic acid group is directed toward the solvent. When deprotonated, it generates high absolute values for the surface potential. The adsorbed amount of citrate ions is pH dependent. Hidber and Gauckler (25) showed that for a powder with surface area of 10 m^2/g, complete adsorption occurred for concentrations under 0.2 weight % in the pH range of 3-7. The isoelectric point could be shifted to 3.4 from 9.1 by the addition of 0.4 weight % citrate. When adjusted for the surface area of the TAL powder, the amount of sodium citrate necessary to achieve the same effects is higher. The equivalent ratio of citrate weight % of 1.7 should shift the IEP to 3.4, but only produces a value of 5.3. The high surface area of the powder provides a greater number of surface charge groups compared to a conventional alumina powder. The higher ionic strength necessary to maintain electroneutrality will screen the electrostatic repulsion between charged surface groups and allow for increased citrate ion adsorption. Therefore, this powder may have a slightly higher adsorption capacity than a conventional alumina. Also, if there is an increased dissolution of the powder, some citrate will form chelate complexes in solution rather than a surface complex.

Within the effects postulated, the behavior of citrate ion as a dispersant is similar to prior investigations. However, the comparison between zeta potential values shows greater differences. Our measurements of zeta potential appear to maximize at -32 mV. Hidber et al. under similar conditions found zeta potential values of approximately -65 mV. In contrast, Dietrich et al. (10) measured values for 20 nm ceria particles and found zeta potential values lower than -40 mV both on the native powder and with the use of polyelectrolyte dispersants, but their ionic strengths are not specified. All three measurements were performed using electroacoustic methods with calibration standards. Hidber and Gauckler studied 500 nm particles, and the larger particle size may be the difference between the values. The low values determined for the nanosized materials raises a potential concern for nanoparticle processing, as loss of electrostatic stability at short range will lead to irreversible aggregation. Estimates of conditions required for nanoparticle stability suggest that electrolyte concentration should be less than 10^{-4} M, and the particle zeta potential should be high (40-50 mV) (29). Ionic strengths of 10^{-3} M or higher were shown to lower the zeta potential value significantly. The amount of dispersant, acid, or base and their associated counterions increase concentration as the amount of water decreases. The result is that at high solids concentration, the background electrolyte concentration can be as high as one molar. Therefore, it is very important to know if high

zeta potential values can be generated under elevated electrolyte levels. The lower values of zeta potential measured here suggest that the powder will not generate strong electrostatic surface interactions.

For a molecular dispersant such as sodium citrate, the steric interaction of the particle is very short range and most of the effectiveness of the molecule is due to the generation of a high zeta potential under alkaline pH conditions. To add the additional steric component to the powder stabilization, polyelectrolytes are commonly used to disperse ceramic powders (30,31). For polyelectrolyte surfactants like Darvan C (which is poly(methacrylic acid)), there is both an electrostatic component to repulsion due to the carboxylic acid groups in the polymer, and a steric repulsion resulting from the polymer conformation. The polymer conformation is a sensitive function of the salt concentration, pH, adsorbed amount, and the system history. Studies of similar surfactants like poly(acrylic acid) show that increasing salt concentrations lower the extension of the polymer from the surface due to screening of electrostatic repulsions between ionized groups on the polymer chain (5-8).

The amount of dispersant needed to form a stable suspension was first considered using a titration of a suspension with the dispersant at pH 9 until a constant zeta potential value was obtained, and the mass of dispersant to the powder was found to be 0.77%. Additional surfactant did not raise the value of the zeta potential, and the titration of this concentration is shown in Figure 4. When suspensions of higher concentration were prepared, it was obvious that the powder was not dispersed. Rheology measurements at 15 volume % TAL alumina were performed to determine the point of minimum viscosity with added surfactant. The dispersant concentration that stabilized the suspension was found in this manner to be 3.16 wt % polymer. Conventional powders have required as little as 0.2 weight % polyelectrolyte to achieve 60 volume % fluid suspensions (32). Clearly the additional surfactant needed to disperse a concentrated suspension is not affecting the electrostatic repulsion between surfaces. Pedersen and Bergstrom has postulated that repeated contacts between zirconia surfaces with poly acrylic acid dispersants led to adhesive forces until polymer was "packed" between the contact zones to form a repulsive barrier (8). The higher required concentration of polyelectrolyte for this powder may result from the need for dense adsorbed layers to resist aggregation from multiple particle collision events.

For the steric Hypermer KD-1 surfactant, the optimum dispersant concentration was determined by measurements of viscosity at 20 volume %. A concentration of 4 wt% surfactant was found to give the lowest viscosity values. This is comparable with the poly(methacrylic acid) concentration required for dispersion. As the molecular weight of the dispersant is proprietary, it is likely that the higher mass ratio relates to a higher molecular weight for the dispersant molecule, and potentially a larger interparticle separation distance.

Rheology of the suspensions with each dispersant were measured for a number of volume fractions. In Figure 6, only the profiles near 30 volume % are shown to indicate the difference in behavior between each dispersant type under similar conditions in solids loading between the surfactants. As the Darvan C surfactant had greater performance than the others, the profile at 37 volume % is also presented. The shear rate measurements show that the behavior of the suspensions looks nearly linear on a log-log plot. The slope in these plots is a function of volume fraction, and at lower solids loading the slope of the log-log plots for the Darvan C and Hypermer KD-1 dispersed systems is very low and exhibits only mild shear thinning behavior. For the sodium citrate and native powder, the rheological response is highly shear thinning at all solid loadings, and suggests that these systems are flocculated. For the dispersed systems, shear thinning is only pronounced at the highest solid contents measured.

The viscosity values at 400 sec^{-1} were used for plotting the behavior of the suspensions against solids loading in Figure 16. Clearly, the polyelectrolyte dispersant (Darvan C) demonstrates the greatest capability for forming high solids content suspensions. The near linear response of the native and sodium citrate suspensions plotted in a semi-log fashion are very similar to behavior of salt flocculated systems (33). Further study of rheological properties is necessary to determine if the suspension behaves according to theories of gelled systems, which are based on percolation theory. The sodium citrate suspension exhibits lower viscosities than the native powder, and the steric length of the adsorbate has been predicted to be approximately 0.5 – 1.0 nm (34,35). As the van der Waals interaction is hyperbolic at very short (< 5 nm) ranges, the adsorption of the citrate ion can be expected to create this reduction in viscosity. Luther et al. observed similar reduction of the viscoelastic properties of flocculated suspensions at the native isoelectric point and at the isoelectric point in the presence of citrate (35).

For the two dispersed systems, shear thinning is observed and a constant viscosity is approached at high shear rates. Plots of high shear viscosity vs. volume fraction are typically fit with a modified Krieger-Doughtery relationship (8).

$$\eta_r = \left(1 - \frac{\phi}{\phi_{\max}}\right)^{-n\phi_{\max}} \tag{3}$$

Here, η_r is the relative viscosity, ϕ_{max} is the maximum solids loading, and n is factor describing the increase in viscosity. The native and citric acid systems could not be fit using this equation, but both the Hypermer KD-1 and Darvan C dispersed suspensions did generate realistic fitting parameters given in Table 2. The rheology data predicts that maximum packing will be achieved for the KD-1 system at 35 volume %, and at 40 volume % for the Darvan C system.

From Figure 16, the slope of the relative viscosity data points away from the maximum packing boundary is very similar between the two dispersed systems. This indicates that both systems are stable until the volume fraction of powder approaches the packing limit. The difference in maximum packing attainable for each system can be attributed to the volume of the surfactant. Dietrich et al. used linear polyelectrolytes and predicted a monolayer thickness of 3-5 nm (10). Under high salt conditions, the electrostatic interaction will be screened, and the dispersant will present a largely steric interaction. Our calculation for a 50 nm particle size correlates well with this result, as the expected true packing fraction for a 5 nm barrier is ~37 volume %. The steric length of the Hypermer KD-1 surfactant is taken to be that of a typical commercial surfactant near 5-10 nm. The lower maximum volume fraction predicted from the rheology data is expected based on these assumptions. A more defined study is needed to characterize these interparticle separations.

CONCLUSIONS

The nanosize alumina powder showed properties similar to conventional alumina materials with respect to phase stability and isoelectric point. The magnitude of zeta potential generated by the native powder surface and in the presence of aqueous surfactants is lower than that typically seen for conventional powders but in agreement with that of nanopowders. The enhanced solubility of the nanopowder leads to some phase transformation, and may be responsible for lower zeta potential values through dissolution and complexation with the surface groups.

In the dispersed state at low solids loading, particle association was modeled from acoustic data, and suggested that particles associate at short range but do not agglomerate. Once agglomeration was initiated by lowering the surface potential, agglomerate size was seen to increase, and the particle association phenomena disappeared. The phenomenon is theorized to result from the particle size distribution, and crystallographic differences that generate variations in zeta potential and van der Waals interactions.

The dispersion of these alumina powders can be achieved using conventional polymeric surfactants, but not with the small molecule surfactant studied here. Based on the sub 100 nm mean particle size, the maximum attainable volume fraction will be limited by the volume of surfactant, and a successful route to forming materials or composites from nanosize powders will need to minimize the volume of the dispersion mechanism. The optimal approach must be resistant to high salt concentrations, adsorb strongly to the powder, and have low steric profile. Additional studies of the rheological properties of sub 100 nm powders is necessary to understand and optimize high solids loading dispersion.

REFERENCES

1. E. Laarz, M. Carlsson, B. Vivien, M. Johnsson, M. Nygren, and L. Bergstrom, J. Euro. Ceram. Soc. 21, 1027 (2001).
2. R.B. Bagwell and G.L. Messing, J. Am. Ceram. Soc. 82, 825 (1999).
3. R.B. Bagwell, G.L. Messing, and P.R. Howell, J. Mat. Sci. 36, 1833 (2001).
4. C.S.Nordahl and G.L. Messing, J. Am. Ceram. Soc. 79, 3149 (1996).
5. N.S. Bell, J. Sindel, F. Aldinger, W.M. Sigmund, J. Coll. Interface Sci. 254, 296 (2002).
6. S. Biggs, T.W. Healy, J. Chem. Soc. Faraday Trans. 90, 3415 1994.
7. H.G. Pedersen and L. Bergstrom, J. Am. Ceram. Soc. 82, 1137 (1999).
8. L. Bergstrom, E. Blomberg, and H. G. Pedersen, Key Eng. Mat. 159-160, 119 (1999).
9. J.L. Deiss, P. Anizan, S. El Hadigui, and C. Wecker, Coll. Surf. A, 106, 59 (1996).
10. A. Dietrich, A. Neubrand, and Y. Hirata, J. Am. Ceram. Soc. 85, 2719 (2002).
11. T. Hinklin, B. Toury, C. Gervais, F. Babonneau, J.J. Gislason, R.W. Morton, and R.M. Laine, , in submission, (2003).
12. A. S. Dukhin and P.J. Goetz, in *Handbook on Ultrasonic and dielectric Characterization Techniques for Suspended Particulates*, edited V.A. Hackley and J. Texter, The American Ceramic Society, 1998, p.77.
13. A. S. Dukhin, P.J. Goetz, and S. Takeda, www.dispersion.com.

14. R. Jenkins and R. L. Snyder, *Introduction to X-ray powder Diffractometry*, Wiley, New York (1996) p. 374.
15. W.H. Gitzen, *Alumina as a Ceramic Material*, The American Ceramic Society, Westerville, OH, 1970. p. 22.
16. S. Kwon and G.L. Messing, Nanostructured Materials 8, 399 (1997).
17. E. Laiti, P. Persson, and L.-O. Ohman, Langmuir 14, 825 (1998).
18. J. Isrealachvili, *Intermolecular and Surface Forces*, Academic Press, New York, 1992.
19. L. Bergstrom, J. Chem. Soc. Faraday Trans. 88, 3201 (1992).
20. W.N. Rowlands, R.W. O'Brien, R.J. Hunter, and V. Patrick, J. Coll. Interface Sci., 188, 325 (1997).
21. N. Kallay and S. Zalac, J. Coll. Interface Sci., 253, 70 (2002).
22. D. Velegol, S. Catana, J.L. Anderson, and S. Garoff, Phys. Rev. Lett. 83, 1243 (1999).
23. R. Kummert and W. Stumm, J. Colloid Interface Sci. 75, 373 (1980).
24. Y. Liu, L Gao, and J. Guo, Coll. Surf. A 193, 187 (2001).
25. P.C. Hidber and L.J. Gauckler, J. Am. Ceram. Soc. 79, 1857 (1996).
26. P.C. Hidber, T.J. Graule and L.J. Gauckler, J. Euro. Ceram. Soc. 17, 239 (1997).
27. Y. Mao and B.M. Fung, J. Coll. Interface Sci. 191, 216 (1997).
28. K.Gotoh, T. Inoue, J. Inada, and M. Tagawa, J. Dispersion Science and Technology 19, 475 (1998).
29. J. Widegren and L. Bergstrom, J. Am. Ceram. Soc. 85, 523 (2002).
30. J. Cersarano III, I.A. Aksay, and A. Bleier, J. Am. Ceram. Soc. 71, 250 (1988).
31. J. Cesarano III and I.A. Aksay, J. Am. Ceram. Soc. 71, 1062 (1988).
32. A. Zupancic, R. Lapasin, and A. Kristoffersson, J. Euro. Ceram. Soc. 18, 467 (1998).
33. J.A. Yanez, T. Shikata, F.F. Lange, and D.S. Pearson, J. Am. Ceram. Soc. 79, 2917 (1996).
34. S. Biggs, P.J. Scales, Y.-K. Leong, and T.W. Healy, J. Chem. Soc. Faraday Trans. 91, 2921 (1995).
35. E.P. Luther, J. A. Yanez, G.V. Franks, F.F. Lange, and D.S. Pearson, J. Am. Ceram. Soc. 78, 1495 (1995).

Chapter 5. The Role of Steric Separation on the Behavior of Flocculated Alumina Nanopowder

INTRODUCTION

As production methods improve, materials are increasingly becoming available in the form of nanopowders. For those methods employing vapor phase or ultrafine spray-synthesis reactions, the dispersion of the discrete particles becomes critical for the use of these materials in coatings or thick film applications. Although the surface chemistry of nanopowders does not appear to be greatly affected at sizes greater than that required for quantized effects to be realized, there are various geometrical interactions between the size of the dispersant mechanism and the particle size which are important for particles under 100 nm in diameter.

As discussed in our prior work, there is a geometrical consideration for the dispersion of nanopowders related to the ratio of the length of the stabilizing mechanism to the particle size (1). For particles under 100 nm diameter, the length of typical stabilizers (i.e. adsorbed polymers) becomes an appreciable length compared to the particle diameter, and therefore lowers the true solids loading which can be dispersed in a solvent. The counter consideration for nanoparticle dispersion is the estimate of the two particle interaction energy. A number of qualitative trends in dispersion rheology are qualitatively explained by the calculation of the interaction energy between two particles to generate a significant barrier to particle agglomeration (2-4). In the case of nanoparticles, the strength of the interaction is predicted to be lower simply due to the size of the materials. It is thus a significant technical issue to explore the relationship between the length of a surfactant layer on a nanoparticle, and relate the predicted interaction energy profile to the bulk rheological properties of a dispersion. To that end, this study is modeled after previous work by Bergstrom, who investigated the properties of flocculated alumina powders of submicron average particle size (5,6). These investigations adsorb fatty acids of varying steric length to the powders in decalin. The monolayers of the fatty acids act as a steric barrier to particle approach, and fix the separation distance of the particles in a van der Waals potential energy well.

The initial consideration must be the calculation of the interaction energy between the particles. Interaction between two particles is considered to be the sum of the van der Waals attraction and any other stabilizing forces, which in this study are steric. Between identically sized particles, these forces can be estimated using the following equations. The van der Waals attraction is given by

$$V_A(D) = -\frac{A_{eff}(D)}{6}\left[\frac{2a^2}{D^2-4a^2}+\frac{2a^2}{D^2}+\ln\left(\frac{D^2-4a^2}{D^2}\right)\right] \quad (1)$$

A_{eff} is the effective Hamaker constant including retardation effects, D is the separation between particle centers, and a is the particle radius.

$$A_{eff}(D) = \frac{3}{4}kT\left(\frac{\varepsilon(0)_1-\varepsilon(0)_3}{\varepsilon(0)_1+\varepsilon(0)_3}\right)^2\frac{3h\omega(n_1^2-n_3^2)^2}{32\pi\sqrt{2}(n_1^2+n_3^2)^{1.5}}F(D) \quad (2)$$

The static dielectric constant is $\varepsilon(0)$, given for particle [1] and solvent [3], with index of refraction (n), and relaxation frequency ω. The term F(D) is given by

$$F(D) = \left\{1+\left[\frac{\pi n_3}{4\sqrt{2}}(n_1^2+n_3^2)^{0.5}(D-2a)\frac{\omega}{c}\right]^{1.5}\right\}^{-2/3} \quad (3)$$

And the steric interaction due to adsorbed fatty acids is represented by

$$V_s(D) = \frac{\pi akT}{\overline{V}_3}\overline{\phi}_2^2(0.5-\chi)(2\delta+2A-D)^2 \quad (4)$$

for the interaction range of layer interaction $\delta < (D-2a) < 2\delta$. The solvent parameter χ, molecular volume $\overline{V}_3$, volume fraction of the dispersant in the layer $\overline{\phi}_2$, and steric thickness δ were all taken from Bergstrom's

calculation for direct comparison (5,6). Figure 17 presents the interaction energy profiles for particles of 50 nm diameter, for the fatty acids used in this study.

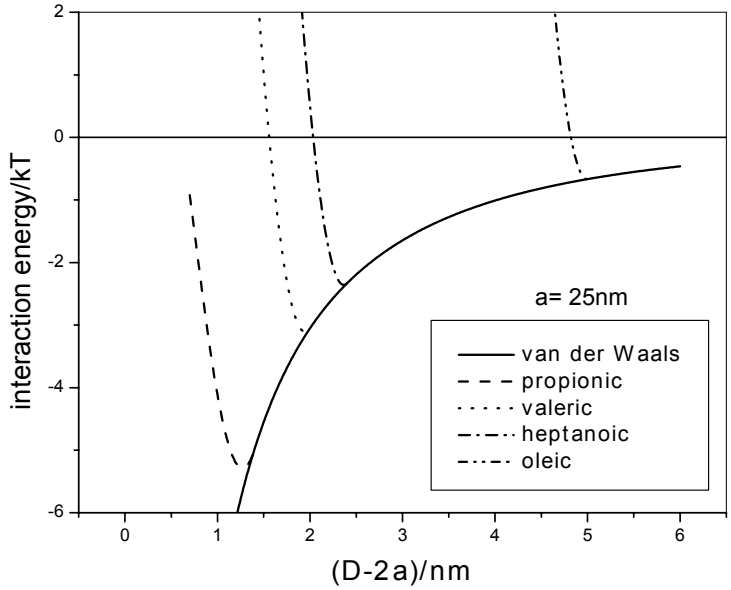

Figure 17 Interaction energy profile calculations for 50 nm diamter alumina nanoparticles, dispersed with various fatty acids.

The calculations indicate that the particles will experience weak short range attractions, varying from 1kT in strength for the study of oleic acid, to 5.4 kT for propionic acid. Of course, this is an estimate for the systems, as the particle size distribution varies from 10 –400 nm with an average size of 50 nm.

A number of investigations have been performed on the formation of particle networks through particle flocculation (5-16). In this study, we examined the rheological response by oscillatory and shear rheology. These measurements show the interplay of interparticle attraction against the reduction in free volume created by the range of the dispersant layer. As this system was previously examined by Bergstrom et al. using larger particle size, this provides a reference point to show the impact of particle size on the flocculated rheological response (1,2). By studying a flocculated system, we can examine the volume fraction dependence of each fatty acid under the theory of a particle gel system.

EXPERIMENTAL

The alumina nanopowder was purchased from TAL Materials (www.talmaterials.com). The propionic (Fisher, 99%), valeric (Avocado, 99%), heptanoic (Aldrich, 99%), and oleic (Aldrich, 99+%) acids were purified by vacuum distillation and refrigerated during storage. Water adsorption was prevent by use of molecular sieves (Fisher, Grade 4A). Decalin (*cis/*trans-decahydronaphthalene, 99%, Aldrich) was stored in darkness and kept sealed throughout experimentation. Solvent was removed by syringe methods for sample preparation. All samples were prepared from the same lot of alumina, decalin, and acid.

Ideal acid concentration for monolayer coverage was estimated from the plateau value of the adsorption isotherms. Adsorption isotherms were measured by the solution depletion method, where 10 volume percent solids loading was prepared in a range of acid concentrations, and the supernatants underwent gas chromatography/mass spectroscopy to determine remaining acid concentrations. The concentration of the acid in the supernatant was plotted against the initial concentration of acid before the powder was added. The weight percent acid adsorbed was determined from the line fit.

For the rheological measurements, the solid loading was varied from 0.15 to 0.35 in the oleic acid samples, 0.1 to 0.25 in the heptanoic samples, 0.08 to 0.2 in the valeric acid samples, and 0.08 and 0.15 in the propionic acid samples. The highest solid loading was limited by the feasibility of loading the rheometer. During sample preparation, the alumina was added to the acid and decalin solution in small increments, then mechanically mixed using spatula and maxi mixer or specs mill with yttria stabilized zirconia mixing media, depending on the ease of

mixing. All samples were mixed at least five minutes on the specs mill before measurement. Samples not immediately measured were refrigerated during storage and mixed before measurement.

In order to achieve consistent rheological testing, samples were tapped or ultrasonicated under vacuum in a syringe in order to collect and remove trapped air bubbles, and then the sample was passed between coupled syringes to further mixing and air evacuation. Samples were loaded directly into the rheometer from the syringe in one coherent mass. To prevent evaporation during measurement, a solvent trap requiring a small amount of lamp oil for sealing was used.

The rheometer used was a cone and plate rheometer (Thermo Haake RheoStress 300, Germany) with a 1˚ cone angle and a 60 mm diameter. The temperature of the plate was maintained at 25 ˚C with a recirculating pump. To ensure identical sample history, each test was preceded by a two minute period of constant shear rate at 300 sec^{-1} for the oscillatory stress sweep measurements or 400 sec^{-1} for the oscillatory frequency sweep and flow curve measurements, followed by 60 seconds at rest. The limits of the viscoelastic regime were determined by a series of stress sweep experiments over a range of 0.4 Pa to 400 Pa, carried out at several constant frequencies from 0.1 Hz to 100 Hz. A 30 second no-shear interval separated each stress sweep experiment, and a 60 second no-shear interval separated the frequency sweep and the shear rate ramp. Frequency sweep experiments were carried out in the viscoelastic region of each sample, over a frequency range of 0.1 Hz to 10 or 100 Hz, depending on the stability of the data at high frequencies. Shear rate ramps ascended from 0 to 400 sec^{-1} in 2 minutes, held constant rotation at 400 sec^{-1} for 30 seconds, and then descended from 400 to 0 sec^{-1} again in 4 minutes. Time dependent properties were eliminated by repetition of shear rate ramps after a 5 minute no-shear interval.

RESULTS

The adsorption isotherm results to determine ideal acid concentration is given in Table 3. These values are compared to the values found by Bergstrom et al., and are in reasonable agreement to their values (5). Our values for adsorbed amount are slightly higher, which likely an effect of the higher curvature inherent to the nanopowder.

Table 3 Adsorption isotherm results for monolayer coverage of TAL Materials alumina nanopowder, and reference information from studies done on conventional powder (5,6).

Dispersant	Adsorbed Amount TAL Materials - %	Adsorbed Amount Bergstrom (5,6)- t%	Steric Length
Propionic Acid	3.22	2.73	0.7 nm
Valeric Acid	3.84	3.25	1.0 nm
Heptanoic Acid	4.06	3.97	1.2 nm
Oleic Acid	6.86	6.39	2.5 nm

Stress sweeps were performed for frequencies of 0.1, 10, and 100 Hz. Figure 18 presents the behavior of the oleic acid and propionic acid coated powder at an intermediate solids loading for each system. The tests with valeric and heptanoic acid were similar to the propionic acid system in viscoelastic response. In the case of oleic acid, there is a weak frequency dependence for the complex modulus, and the viscoelastic region increases slightly with increasing frequency. The upper stress boundary of the viscoelastic range for the oleic acid data is marked by a descent from the constant value found at low stresses. The upper stress limit of the viscoelastic range was less well defined for the oleic acid data than for the other acid types.

For the case of the propionic acid coated particles, the elastic modulus (G') values are nearly two orders of magnitude higher than the oleic acid case. They are effectively constant with their frequency response. The propionic case exhibits the opposite behavior with respect to the breakdown of the linear elastic region. The end of the viscoelastic range was marked by a steep drop from well defined constant value in both modulus curves. Higher frequency tests cause breakdown at lower stresses. The loss modulus (G'') curve typically mimicked the elastic modulus curves with a lesser magnitude and showed greater spread. A stress value below the limiting upper boundary of the viscoelastic range, where the elastic modulus appeared independent of stress, was chosen individually for each sample and used in the oscillatory frequency sweep experiments.

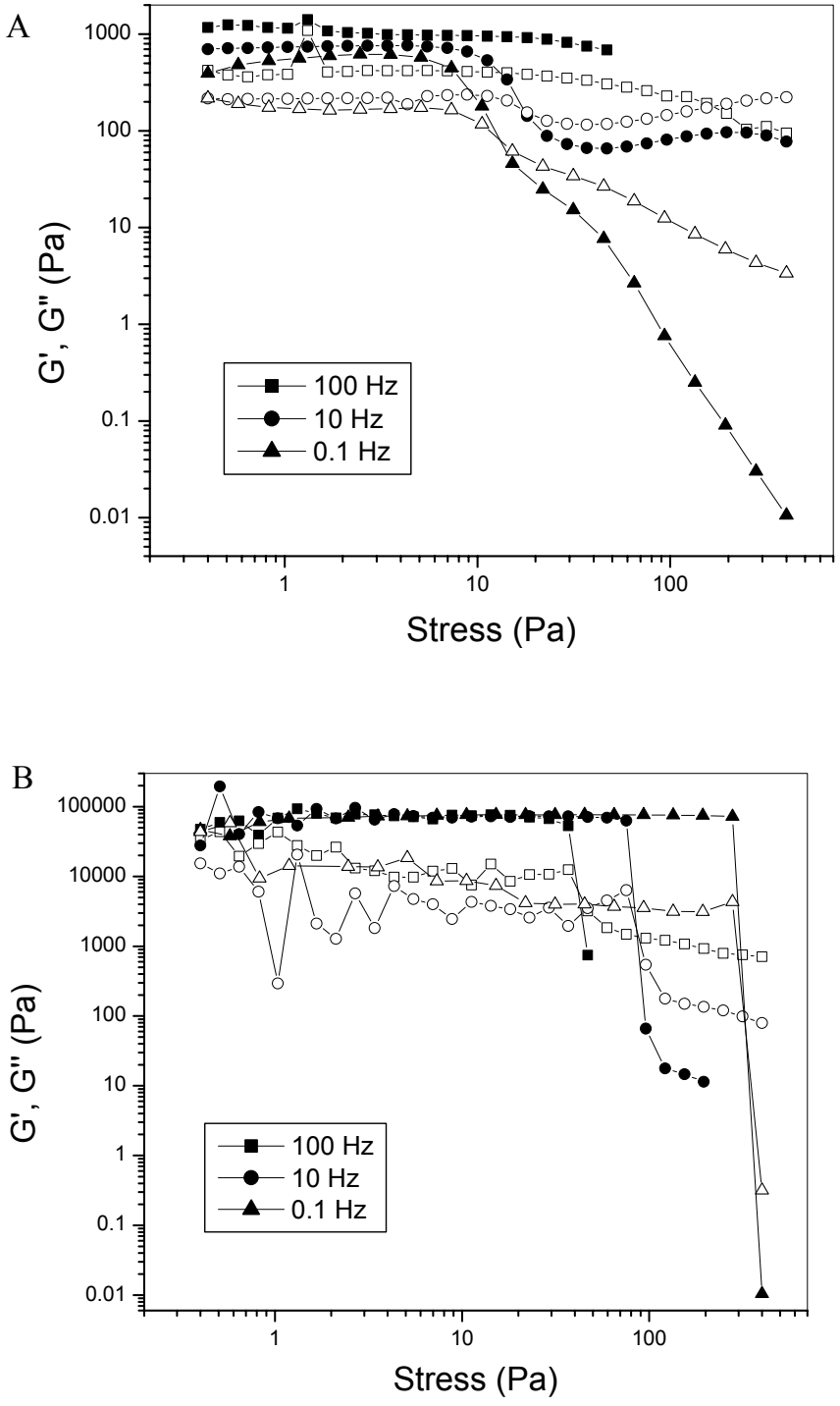

Figure 18 A. Stress dependence of moduli in ϕ=0.25 oleic acid sample. B. Stress dependence of moduli in ϕ=0.12, propionic acid sample. Filled symbols are G' and empty symbols are G".

Figure 19 contrasts the volume fraction of solid phase for the oleic and propionic acid coated systems. The oleic acid series was measured from solid contents of 15 to 35 volume %. At low solids loading, the data indicates a fluid response (i.e. $G'' > G'$), and as solids loading begins to exceed 22 - 24 volume %, the elastic modulus

becomes greater than the loss modulus. As stress increases, the elastic response undergoes a transition to fluid behavior. At the highest solids content measured, the transition from elastic to viscoelastic behavior gives approximately equivalent values for G' and G''.

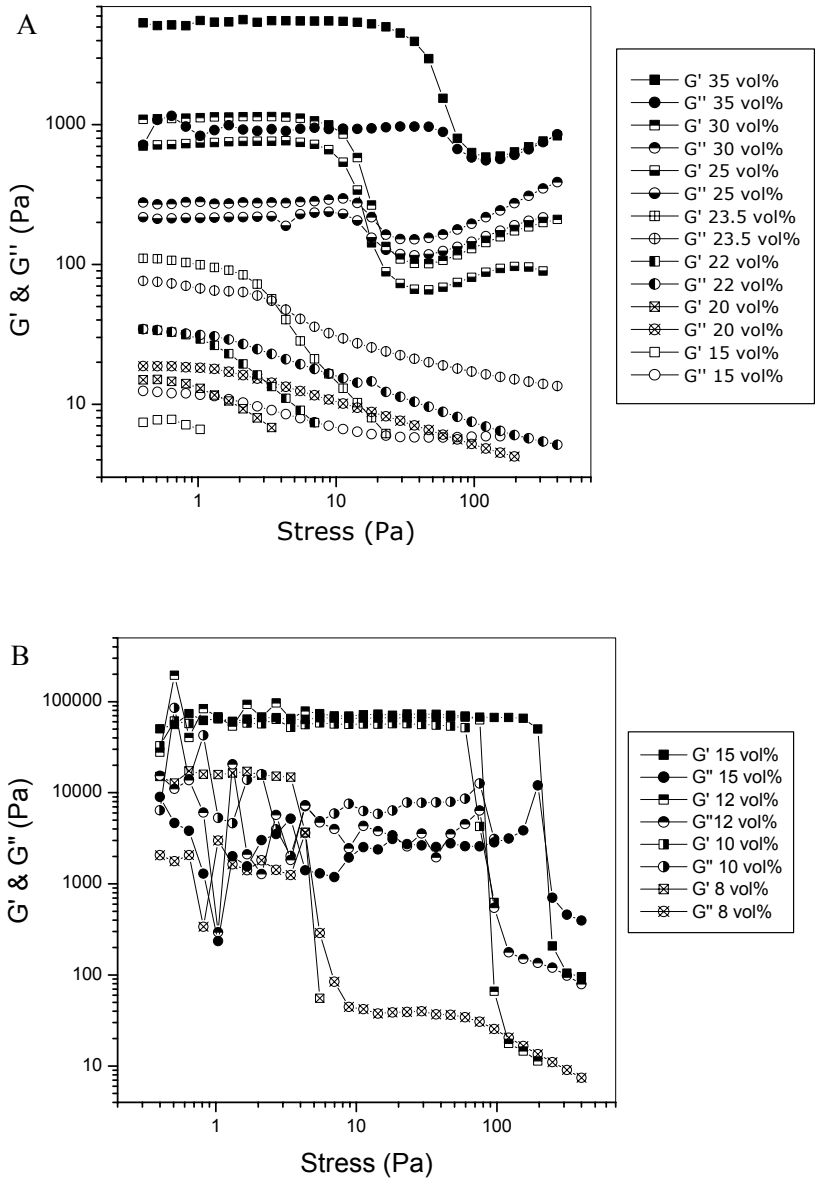

Figure 19 A. Stress sweep curve dependence on particle concentration for oleic acid. B. Stress sweep curve dependence on particle concentration for propionic acid.

The other acids, as typified by Figure 19B showing propionic acid stress sweeps at 10 Hz, displayed only elastic behavior. The general trend of an increase of modulus value by particle concentration was repeated, but the propionic acid data exhibits a ceiling modulus value at ϕ=0.10. The elastic modulus values for the flocculated systems are more than an order of magnitude higher than the oleic acid case, and are generated at much lower nanopowder concentrations, ranging from 8 to 15 volume %. This series also exhibits the catastrophic breakdown of elastic behavior as stress increases, with the elastic network strength rising with solids loading. Both the valeric and heptanoic acid coated particles exhibited similar response to the propionic case, but were able to form higher solids loading samples.

The stress sweep curves were used to estimate the limit of linearity for each system as a function of the effective volume fraction. The limit of linearity is defined as the strain at which the elastic modulus drops below 95% of the maximum elastic modulus. In Figure 20, the limit of linearity exhibits a transition in behavior from rising with particle concentration in the flocculated systems, to falling with concentration for the oleic acid coated nanoparticles.

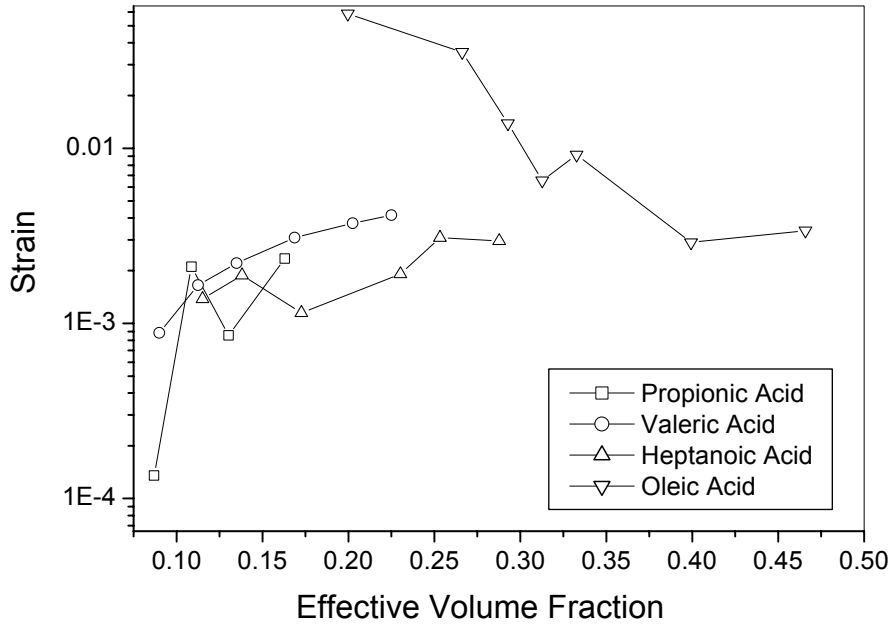

Figure 20 Limits of linearity as a function of volume fraction for the fatty acid coated alumina nanopowder.

An estimate of the elastic strength as a function of volume fraction was taken by averaging the data within the viscoelastic range from the 10 Hz tests, which shows the dependence of the elastic modulus on particle concentration for each fatty acid series of suspensions. For the response where there was no appreciable constant region, the lowest G' value was assumed to represent the elastic character. As expected, the elastic modulus increases with volume percent solids. Figure 21 presents the response for each series of measurements. The flocculated systems were fit with a percolation theory model, which is described in the discussion section.

Frequency sweep measurements in the linear elastic region were performed for each system. Figure 22A shows the response of the oleic acid system, and Figures 22B-D present the propionic, valeric, and heptanoic acid systems. The data in these systems was fit with a Freidrich Braun model for the frequency response of the suspension, and the equations follow (17). This model is a fractional derivative model where c and d are the derivation orders.

$$G'(\omega) = G_\infty + \Delta G \frac{(\lambda\omega)^d \left[\cos\left(d\frac{\pi}{2} \right) + (\lambda\omega)^c \cos\left((d-c)\frac{\pi}{2} \right) \right]}{1 + 2(\lambda\omega)^c \cos\left(c\frac{\pi}{2} \right) + (\lambda\omega)^{2c}} \tag{5}$$

$$G''(\omega) = \Delta G \frac{(\lambda\omega)^d \left[\sin\left(d\frac{\pi}{2} \right) + (\lambda\omega)^c \sin\left((d-c)\frac{\pi}{2} \right) \right]}{1 + 2(\lambda\omega)^c \cos\left(c\frac{\pi}{2} \right) + (\lambda\omega)^{2c}} \tag{6}$$

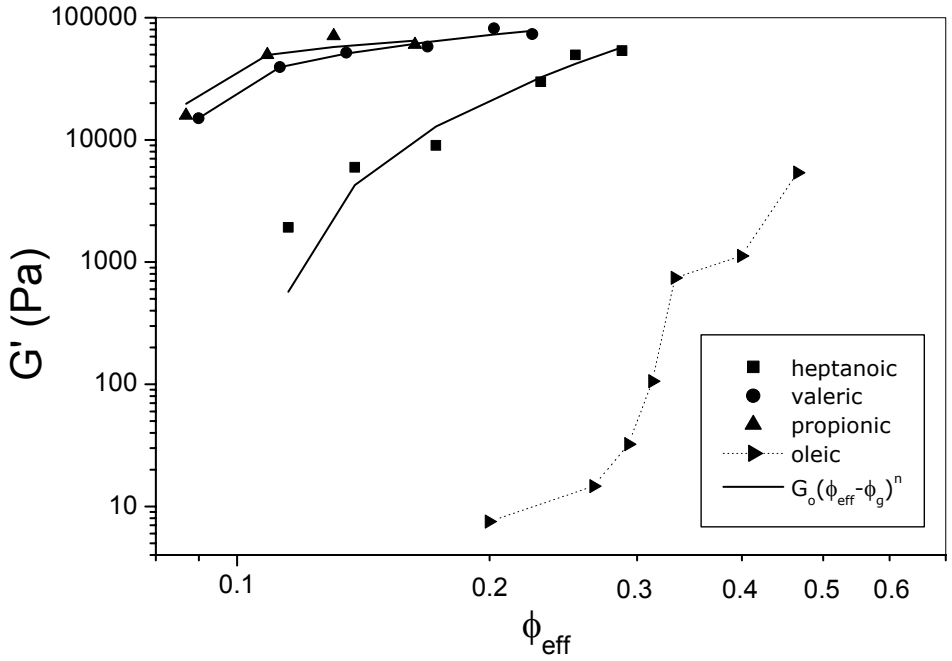

Figure 21 Elastic modulus dependence on effective particle concentration for all acids. Solid line represents best fit of eqn (7), dotted line is given to guide the eye.

G_∞ is the equilibrium modulus as frequency approaches zero, and λ is the characteristic time of a material, which determines the role of the elastic and viscoelastic components in the response. For c = d = 1 and G_∞ =0, λ becomes the relaxation time in the Maxwell model. The propionic acid curves could be well approximated only by the elastic modulus relation, the valeric acid data was poorly described by the model, and the heptanoic data showed reasonable correlation. The oleic acid data was well described by the Freidrich-Braun model. The parameters for these equation fits are given in Table 4.

Figure 22A displays the frequency sweep data for varying values of particle concentration in oleic acid. The frequency response of the system is very similar to that presented by Zupancic et al (18), but with larger modulus value magnitude. Both the elastic modulus (G') and the loss modulus (G'') increase with increasing solids loading, and the system shows a trend towards increasing elasticity and decreasing viscous behavior with increasing solids loading. The highest solids loading shows essentially elastic behavior over the entire frequency spectrum, while the lowest solid loading is essentially liquid-like. Within the solids loading range of 0.2 to 0.3, a clearly defined crossover of the curves is apparent. The material flows at low frequency and displays elastic behavior at frequencies above the crossover. As the solids loading is increased, both moduli show strong variation. The elastic modulus shows a trend from increase with frequency at low solids loading to being nearly constant at high solids loading. A more dramatic variation appears in the loss modulus, which changes from steady increase with frequency at low particle concentration to a decrease to an asymptotic minimum at high particle concentration.

The trends in the curves of the other acids were not as well defined. In Figure 22D, heptanoic acid samples followed similar trends to that of oleic acid that were less pronounced, but no data was obtained at low enough particle concentrations to see crossover from viscous to elastic behavior: all samples were largely elastic in nature. Elastic modulus values generally fell in a range roughly four orders of magnitude higher than the oleic acid curves, and loss modulus values were roughly three orders of magnitude higher than the oleic acid curves.

Table 4 Fitting Parameters to the frequency sweep measurements using the Friedrich-Braun model (equations 5 & 6).

Propionic Acid					
ϕ	G_∞	ΔG	c	d	λ
0.15	0	41928±	1±0.18	0.86±0.19	19.89±6.41
0.12	0	57875±	0.98±0.33	1±0.35	16.0±6.03
0.10	0	58595±	0.996±0.07	0.69±0.11	3.17±0.86
0.08	0	16783±	1±0.12	0.96±0.16	5.18±1.43
Valeric Acid					
0.20	0	79546±	1±0.29	0.10±0.06	0.09±0.03
0.18	0	78850±	1±0.25	0.09±0.03	0.06±0.02
0.15	0	70157±	1±0.06	0.97±0.07	8.03±0.67
0.12	0	56812±	0.84±0.11	0.81±0.12	9.99±1.69
0.10	0	27935±	0.82±0.19	0.89±0.21	18.6±3.96
0.08	0	20005±	0.92±0.16	0.97±0.18	19.1±3.59
Heptanoic Acid					
0.25	26558±5522	29157±3729	0.72±0.11	0.74±0.12	4.68±1.17
0.22	17419±2329	21087±1841	0.91±0.10	0.99±0.11	4.25±0.71
0.20	17307±7426	14285±4112	0.95±0.23	1±0.30	6.00±1.78
0.15	6620±3407	8629±2370	0.92±0.30	1±0.36	7.77±3.14
0.12	4900±1742	4708±837	0.91±0.20	1±0.26	3.80±1.29
0.10	1374±354	1581±416	0.90±0.17	1±0.18	10.87±5.22
Oleic Acid					
0.35	0	6790±0	0.93±0.07	1±0.07	4.79±0.63
0.30	619±393	749±201	0.85±0.18	1±0.20	2.46±2.5
0.25	88.3±94.0	142±31	0.76±0.34	1±0.36	1.68±3.03
0.235	4.05±14.37	33.28±10.0	0.69±0.27	1±0.29	1.47±2.1
0.22	3.70±18.87	11.48±21.1	0.63±0.64	1±0.67	3.59±22
0.20	0.35±5.97	3.80±10.4	0.55±0.88	1±0.90	3.66±24.7
0.15	0	2.85±0	0.42±0.03	0.93±0.03	0.49±0.02

The oleic acid curves covered a much wider ranger of modulus values over the range of particle concentrations: for solids loading of 0.15 to 0.35, the range of the elastic modulus data covered 5 orders of magnitude. Heptanoic acid data covered a particle concentration range of 0.1 to 0.25 and a little more than one order of magnitude range in the elastic modulus. Valeric acid data and propionic acid data, had particle concentration ranges from 0.08 to 0.20 and 0.08 to 0.015 respectively, and elastic modulus ranges of only 1 order of magnitude. The modulus values showed a much smaller dependence on particle concentration and had magnitudes quite a bit larger than those of the oleic acid samples. Valeric acid and propionic acid also seem to reach a ceiling value for the elastic modulus at 0.15 and 0.12, respectively. The loss modulus values for these two acids show a great amount of random uncertainty and general trends for these data are difficult to describe.

Figure 23 shows the λ parameter from the Friedrich-Braun equation modeling for each acid series. As the dispersant length increases, the network relaxation time becomes less volume fraction dependent until it is approximately uniform for the oleic acid system.

The oleic acid case displayed behavior similar to that of a dispersed system. The behavior of the dispersion generally shows little hysteresis between the rising and descending shear rate ramps, with an exception for 30 volume %. That sample showed some rate induced breakdown in response to the rising stress, and the recovery was uniform. Both tests at 30 and 35 volume % powder generated torque overstress conditions in the rheometer that prevented collection of data over the entire desired shear rate range. The stress vs. shear rate data was fit using the simple Casson equation.

$$\sqrt{\tau} = \sqrt{\tau_y} + \sqrt{\dot{\gamma}\eta_0} \tag{7}$$

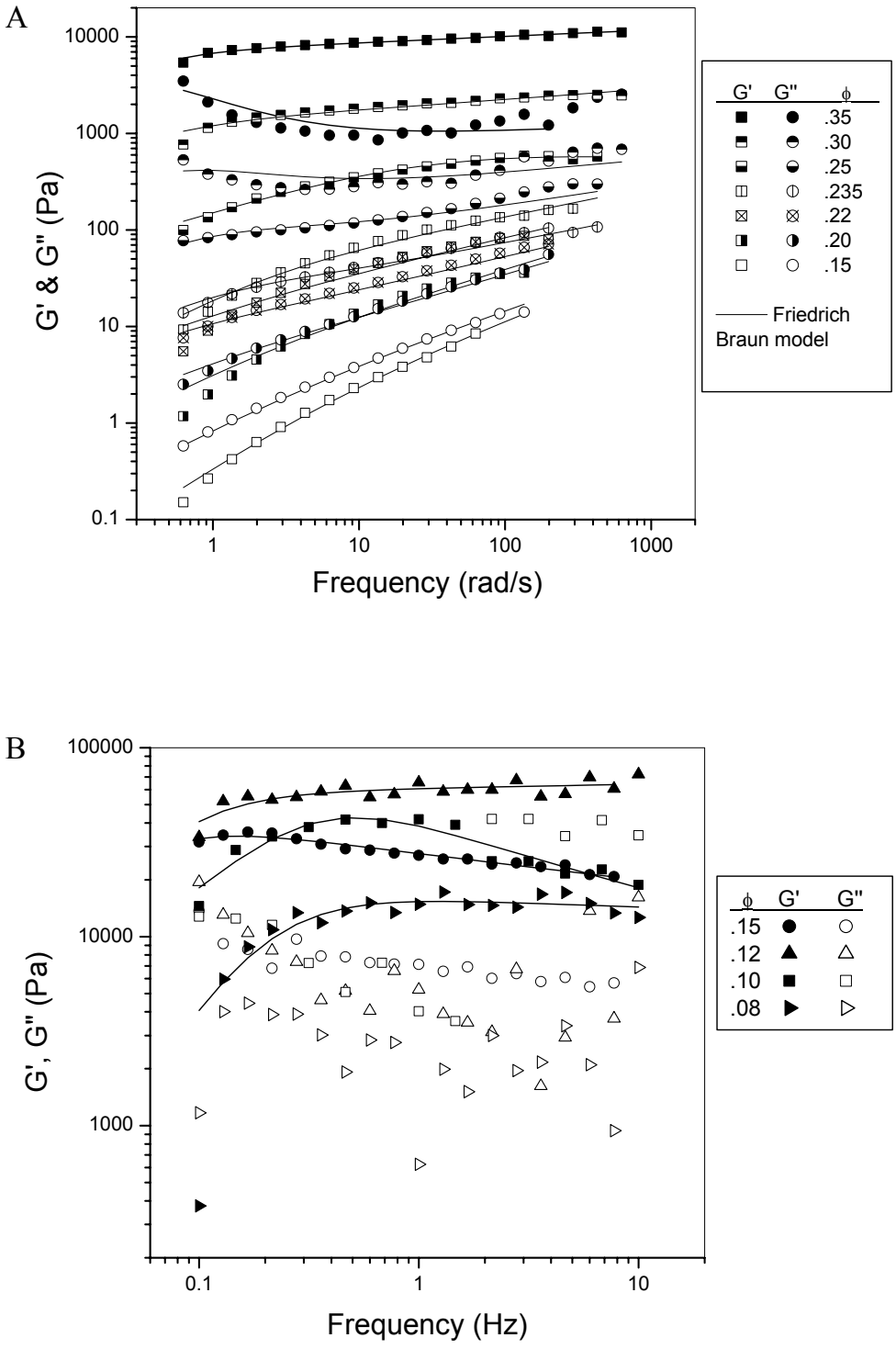

Figure 22 A. Dependence of frequency response on particle concentration for oleic acid. B. Dependence of frequency response on particle concentration for propionic acid. Solid lines represent the best fit of the Friedrich Braun model, for elastic modulus only (eqn 5). Parameters are given in Table 2.

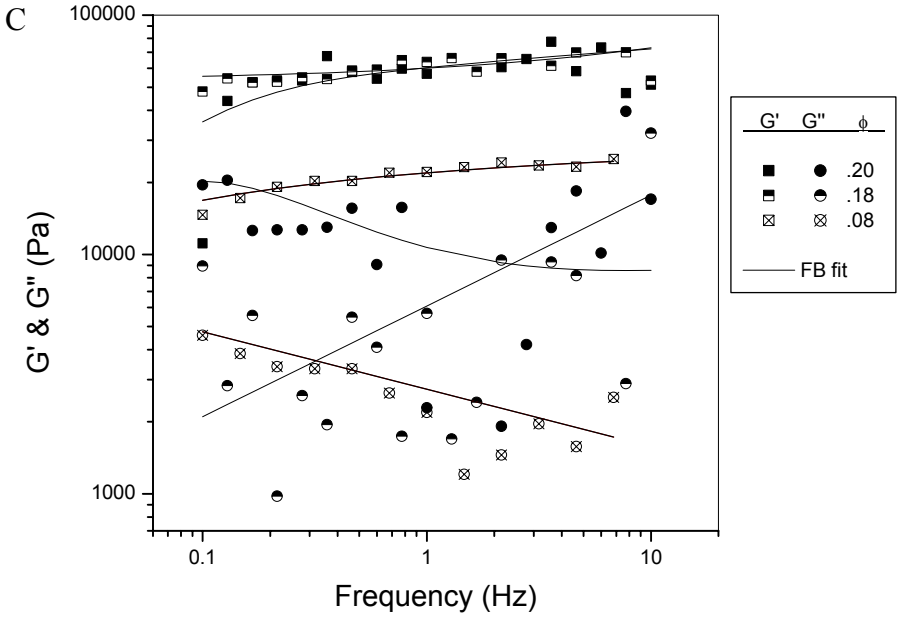

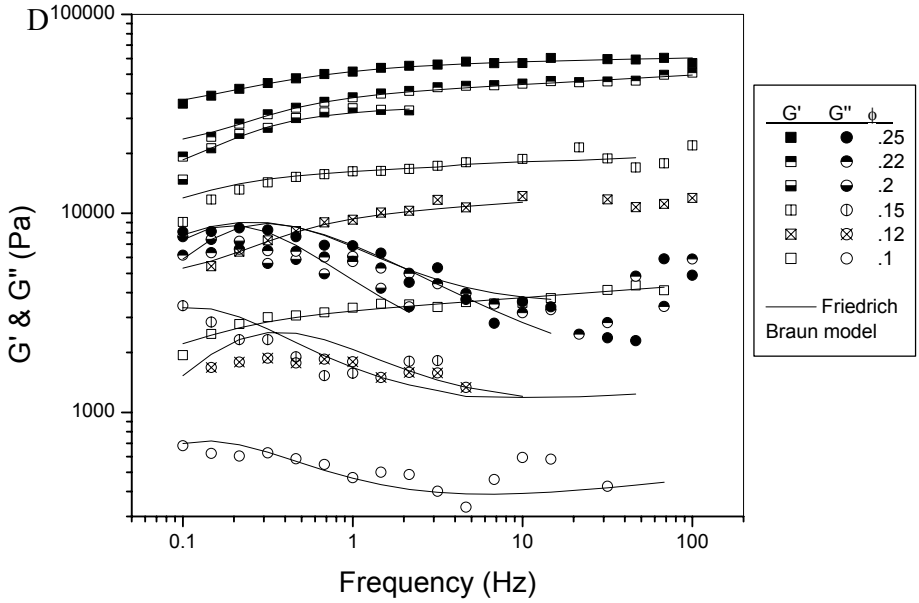

C. Dependence of frequency response on particle concentration for valeric acid. D. Dependence of frequency response on particle concentration for heptanoic acid. Solid lines represent the best fit of the Friedrich Braun model, for a simultaneous fitting of elastic and loss moduli (eqns 5,6). Parameters are given in Table 2.

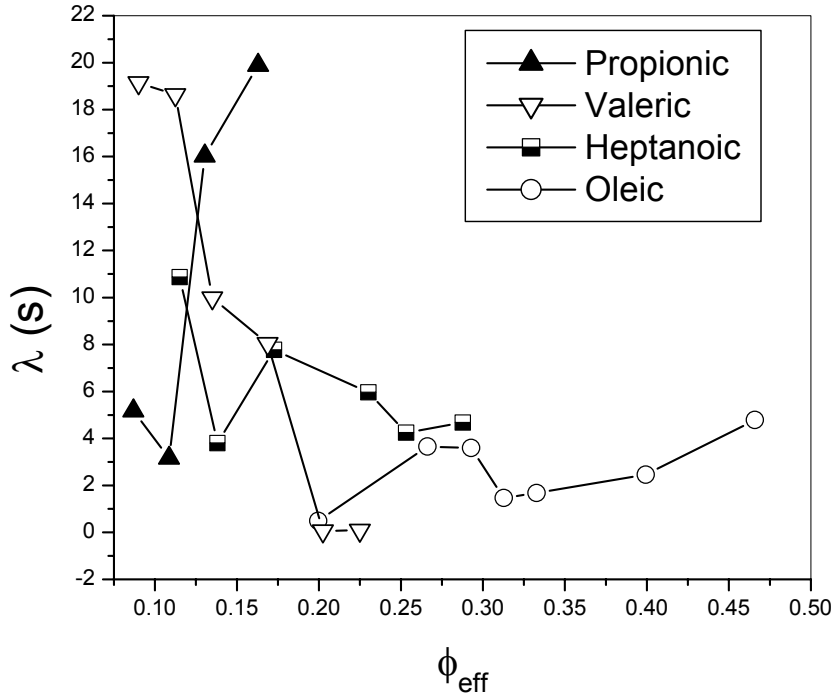

Figure 23 Relaxation time parameters calculated from Friedrich-Braun Modeling of frequency sweep data for each fatty acid coated system.

Table 5 Fitting parameters for the shear stress vs. shear rate data in the oleic acid dispersed alumina nanopowder system.

Volume Fraction	τ_y *(Pa)*	η_0 *(mPas)*
0.35	75.01	5.01
0.30	24.2	2.71
0.25	13.3	1.41
0.235	5.0	0.34
0.22	3.13	0.24
0.20	1.94	0.22
0.15	0.84	0.23

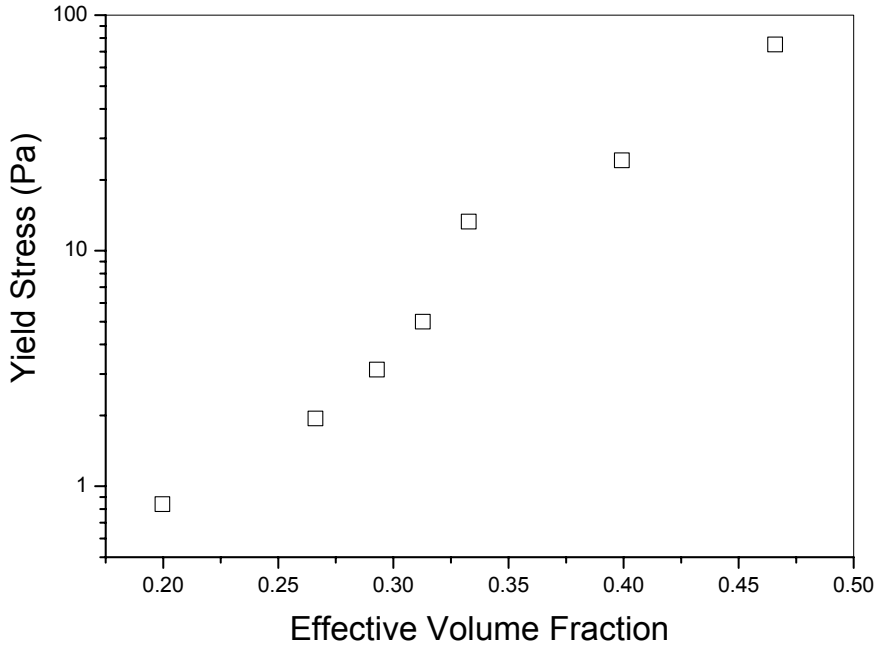

Figure 24 Yield stress vs. effective volume fraction for the oleic acid system.

The yield stress τ_y and intrinsic viscosity η_0 are determined by the least squares fitting of the shear stress vs. shear rate data. The parameters for fitting the data is given in Table 5, and Figure 24 presents the yield stress graphically. The profile of the yield stress vs. the effective volume fraction has an approximately linear form in the semi-log plot. The continuing log response of the yield stress suggests a maximum packing fraction of 50-55% including the length of the oleic acid monolayer.

DISCUSSION

The focus of these experiments is to determine the relationship between the steric thickness of a dispersant layer and the resulting rheological properties of the nanoparticle dispersion. This will determine a minimum length for dispersants used to prepare nanoparticle materials in high solids content suspensions. Based on the interaction energy diagrams calculated for the series of fatty acids, it is expected that the behavior of the system will transition from a flocculated particle gel with strong interactions to a system that behaves with weak attractive interactions. To confirm the behavior of the various systems, we examine the data within the framework of particle gel theory.

Particle gels are formed by aggregation events, and Grant and Russel first applied concepts from percolation theory to scaling the elastic properties (9). Shih et al. then scaled the elastic properties analogously to the development of polymer gels in semi-dilute solution, as they argued that the formation of fractal floc units is controls properties beyond the gelation threshold (19). The structure of the particle gel is dictated by the rate of particle aggregation, and two behavioral extremes are predicted. If the potential for flocculation is weak, several flocculation events may be required for attachment to occur and aggregation is considered reaction limited. Conversely, if the probability for aggregation is unity for each two-particle collision, the aggregation mechanism is limited by the frequency of particle collisions, and aggregation is diffusion limited. The development of floc structure by reaction limited cluster aggregation (RLCA) and diffusion limited cluster aggregation (DLCA) have been simulated by a number of studies to see the impact of aggregation probability on the resulting structure. These structures are characterized by their fractal dimension, and the fractal dimension of each rate law is 1.75 and 2.0 respectively (20-25). Other simulations have found that in concentrated systems, the DLCA fractal value decreased to 1.4 (26).

Fundamental studies of flocculated systems generally focus on systems in which dispersion can be controlled by external control of the environment, such as with temperature (5-14). In this way, flocculation is

induced by changes in wetting between surfaces, or the solubility of the dispersant layer in the solvent. There is some argument regarding the optimal treatment for scaling the elastic properties of the particle gel. The fractal aggregation models do not require a minimum particle concentration to span the system, and have rate laws that are well documented in fundamental studies (19-26). The energy dependence of the fractal dimension was shown by Liu et al. to lie near 2.6 for strong interactions (near 4 *kT*) and decrease toward 1.8 as the interaction energy is reduced (24). Several studies claim that percolation theory can approximate the behavior of true particle systems more accurately (8,9). Percolation theory applies the concept of a minimum value of particle concentration to span the system, and several theoretical predictions of the percolation threshold predict a value of 16 volume % (27). However, there are examples in the literature of gels with much lower particle concentration. Allain et al. found for sedimenting $CaCO_3$ nanoparticles, that the particle network had sufficient strength to resist gravity induced collapse at a particle concentration of ~5 volume % (28). That study was flocculated by processing at the isoelectric point, so that van der Waals attraction was the attractive force. Grant and Russel found in their temperature dependant system that particle concentrations as low as 0.001 would gel if the temperature was low enough (9). Shih et al. found a gelation threshold at $\phi = 0.02$ in boehmite gels, although it should be noted that their particles were platelets (19). These sources imply that as interaction becomes stronger, the gelation threshold should decrease.

The rheological properties of flocculated systems are related to the structure formed by the aggregation events, the interparticle and interfloc bond strengths, and the floc characteristic size. Each nucleating particle aggregate is characterized by a fractal dimension, and a gel is considered a packed network of these fractal aggregates. The gelled network can then be described as either a strong link or weak link network, in which (1) G' increases more slowly in the weak link regime and (2) the limit of linearity increases with increasing particle concentration in the weak link regime, but decreases with ϕ in the strong link regime. Properties that are scaled and compared with the theory include the limit of linearity in the elastic modulus, and the elastic modulus magnitude as a function of volume fraction.

In Figure 20, the limit of linearity is defined as the decrease in the maximum value of G' as strain increases. Only the valeric acid system shows a smooth increase in strain at the point of 95% max G'. The data shows a trend from unstable but increasing values of strain at the point of failure, to the behavior of oleic acid which is predominantly decreasing in strain as the particle concentration increases. Clearly, in the flocculated samples, the limit of linearity increases with particle concentration, and this indicates that the particles are in the weak link regime of aggregation. The oleic acid coated nanoparticles have a decreasing limit of linearity, but their rheological response is more like that of a disperse system than a particle gel, so that system will not be further modeled as a flocculated network. The oleic acid system will be considered separately after discussion of the flocced systems. Under the fractal aggregate theory with reaction limited cluster aggregation, the relationship between the fractal dimension of the flocs and the limit of linearity is of the following form (19).

$$\gamma_0 \propto \phi^{(1)/(3-d)} \tag{7}$$

The fractal dimension of the flocs is represented by *d*, and is determined from the aggregation mechanism and any structural reorientation in the floc. The data for each system was fit with a power law expression, and the resulting exponential factors were equated with the exponent expression in equation 7. The resulting fractal dimensions are included in Table 6 as d_{limit}. The fractal dimensions are within the range of predicted theory, and decrease as the steric length increases. Liu et al. have measured fractal dimensions in this range as a function of the attractive interaction and considering particle rearrangement (24,25). The calculations performed on our data for the interaction energy are also similar to the values predicted by Liu et al. The data suggests that as the interparticle attraction strength increases, the fractal dimension also increases. It should be noted that the data fits generally have a large error coefficient due to the scatter in the data.

Viscoelastic properties are scaled with volume fraction in percolation theory through a power law expression based on the percolation threshold.

$$G = G_0(\phi - \phi_g)^s \tag{8}$$

The prefactor G_0 is related to the particle interaction, ϕ_g is the gelation threshold, and *s* is the power law exponent related to the floc structure (and by extension the aggregation mechanism). Figure 21 presents the behavior of the elastic modulus for each data series as a function of the effective volume fraction, where the effective volume fraction incorporates the thickness of the dispersant layer in the average particle dimension. It is clear that the trend in the particle data follows that expected from the interaction energy diagrams. As the steric length of the dispersant layer increases, the elastic modulus decreases and the attainable particle concentration is raised.

The fitted curves in Figure 21 are based on equation (8), and the percolation threshold and power law exponents are given in Table 6. Fitting of G' data vs. volume fraction generally produced better curves under the assumption that there was a minimum percolation limit for particle volume, as previously shown in particle networks (8). The theoretically predicted values for the exponential power for DCLA is 3.5 ± 0.2 and for RCLA is 4.5 ± 0.2 (29). The fitted values for *s* are much lower than predicted. Although lower values than theoretical have been observed (9), the values found here are beyond the expectation of the theoretical models and other studies (19-22,24). In fact, the propionic acid coated particles are nearly constant in G', and the threshold volume fraction for this constant values appears to occur at $\phi = 0.10$. The percolation thresholds for the data are all below the theoretical value of ~0.16, but greater than the 0.05 value of Allain et al. (23). They do not follow the expected trend of lower ϕ_g with increase in interparticle attraction. These nanoparticle gels are much less dependent on volume fraction for their elastic response, although their limit of linearity is volume fraction dependent.

The fractal aggregate theory for the scaling of the elastic modulus in the weak link regime is of the form

$$G' \propto \phi^{(1)/(3-d)} \tag{9}$$

The power law exponent was equated to this expression for the fractal dimension (equation 9). Table 6 gives the result of this calculation for the fractal dimension of the structural units in each flocculated system as $d_{elastic}$. These values are unrealistic or impossible to consider valid.

Table 6 Fitting parameters for the propionic, valeric and heptanoic acid elastic modulus as a function of solids fraction.

	ϕ_g	*s*	d_{limit}	$d_{elastic}$
Propionic Acid	0.087	0.22	2.47	-1.55
Valeric Acid	0.087	0.40	2.287	0.5
Heptanoic Acid	0.107	1.47	1.966	2.32

With respect to the limit of linearity and the elastic modulus scaling, there is a large discrepancy in the predicted structure. The propionic case is the most difficult to reconcile, as the limit of linearity derived fractal value is greater than that predicted by RLCA, and the elastic modulus prediction is negative. The valeric acid system is also difficult to explain within the framework of particle gel theory for the same reasons. The heptanoic acid case shows good response with respect to the limit of linearity derived fractal dimension, which is very close to that predicted by RLCA, and with elastic modulus data that is not greatly out of bounds. Clearly, there are differences in these systems from the systems previously studied.

The features that make fitting the data so problematic generally relate to the elastic modulus data. It is curious that the flocculated systems exhibit such high values for elastic modulus at very low solids volume and with the relatively low potential energy wells calculated using the van der Waals and steric interactions. Ogden and Lewis performed studies of the relationship between viscoelastic properties and predicted interaction energy curves (30). For their work using depletion flocculation, they calculated attractive potentials of 2-15 kT units, but their measured elastic modulus values are several orders of magnitude lower than the flocculated systems tested in this work, whereas their average particle size is submicron rather than <100 nm. Additionally, several of the thermally unstable systems have elastic modulus values which are much lower and more sensitive to volume fraction (8,9,14). There must be a new phenomenon causing the anomalously high elastic modulus values seen in these studies.

A possible explanation relates to the fabrication method used in sample preparation. These systems were not made via destabilization of the dispersing forces, like that of previous fundamental studies. This method of powder dispersion relies on hydrodynamic forces and mixing. This creates two potential structural effects in the system. The first is the ordering effect of hydrodynamic forces on particle structure. It is known that hydrodynamic forces can result in the formation of string-like particle agglomerates. Vermant et al. have observed the formation of string phases formed by high shear hydrodynamic forces, and the formation of bundle-like formations in very dense suspensions (31). At higher volume fraction and shear rate, hydrodynamic many-body interactions become more important, and the role of the fluid phase must be considered. Although these observations were made in unaggregated particle systems, the effect of hydrodynamic forces on the development of particle structure should be similar. The mechanical shear methods used in the fabrication of these samples may have induced the formation of string-like networks for the flocculated systems. A structure of that type would explain the high values of the elastic modulus for very low solids loading gels such as the propionic and valeric acid cases.

The second effect relates to the strength of attraction between nanoparticles. The potential energy diagrams predict that the attractive force with propionic acid monolayers is relatively weak at 5-6 kT units. It seems unusual

that these strengths would be strong enough to provide the measured elastic modulus values seen in the propionic acid case. As these samples were prepared using mechanical agitation, it is likely that dissolved gasses are present in the solvent. Higashitani et al. have measured the impact of gas bubbles at interfaces, and also the development of bubbles at particle contacts (32,33). They have shown that attractive forces can be significantly long range, strong, and persistent when dissolved gas is present in the solvent. It is also possible that residual bubbles are large enough to act as a second phase. In this study, low vacuum was applied to remove large air bubbles, but it is not likely that all gas was removed. Therefore, for the nanopowder studied here, an additional attractive force due to capillary interactions related to gas bubble formation at interfaces can be reasonably postulated. The removal of these forces is inherently difficult. Higashitani et al. went through extensive freeze-thaw methods to remove gas from the solvent in their studies, and it is unlikely that these procedures are practical for nanopowder dispersion. However, it should be noted that as the steric length of the surfactant increases, these effects are minimized.

To understand the structural relationships, study of the aggregate structure using scattering theory has often been applied. For dispersions of this type, light scattering methods will require dilution to very low particle concentrations. Another approach would utilize neutron scattering, which should be able to measure characteristics at higher solids content. These measurements are beyond the scope of this study, but will be pursued in a future publication.

Oleic Acid-Nanoparticle Dispersion

The use of oleic acid created behavior more similar to a dispersed system than a flocculated one. The behavior of the oleic acid system indicates that nanopowders can be dispersed using molecular dispersants with significantly long steric profiles. The oleic acid system does not appear to be significantly affected by the presence of dissolved gas. It achieved fluid flow behavior in a similar manner to the systems investigated previously (1), with relatively high solid loading and much lower elastic modulus. The system still reaches a maximum at a solids loading below that predicted by the effective solid loading argument. For a 50 nm powder with a 2.5 nm steric surfactant length, it is expected that the maximum solids loading will be near 50 volume %. The effective volume fraction is assumed to be 64%. It is still unclear why the volume of solids does not achieve values closer to this theoretical prediction.

The shear rate response is in agreement with the interparticle energy calculations, which predict that the attractions in this system are only -1kT. The nanoparticle suspension does display some non-characteristic behavior that deviates from expected behavior for hard sphere systems. In the stress sweep studies as a function of volume fraction, it is found that the elastic behavior begins to exceed the viscous behavior at relatively low volume fractions between 22 and 24 volume %. As this system does not have an electrostatic or long range repulsive force, it must be assumed that some form of network structure is formed by the nanopowder, although the network strength is weak as a result of weak attractions between particles. Marshall and Zukoski showed that as the volume fraction increased about 20%, shear thinning develops at a characteristic stress dependant on particle size and volume fraction (34).

The profile of the yield stress and the high shear viscosity also do not conform to the excluded volume models for particles systems (typified by the Krieger-Doughtery or Quemada models) (35-38). After the elastic properties of the network begin to exceed the viscous component, the yield stress and the viscosity increase in a logarithmic manner rather than according to an asymptotic approach to a maximum packing fraction. This is the cause of the torque overlimit restrictions we found in the shear rate sweep experiments for 30 and 35 volume % powder. For these tests, the effective volume fractions were 40 and 46%, proving that the nanopowder was approaching high packing fractions. An explanation for this trend will require further study.

One potential explanation lies in the strength of interaction between the nanoparticles or the flocculated units. Raynaud et al. used the response of the elastic modulus with volume fraction to estimate the interparticle potential in a system of dispersed particles (35). Their study also approximates the effect of the surfactant thickness on the achievable maximum solids loading. However, it is unknown if there are similar equations relating the properties of flocculated systems to the elastic modulus. Mewis describes the rheological properties of sterically stabilized particle systems (36). In these systems, the Zwanzig-Mountain equation can be used to relate the plateau modulus G_∞ to the interaction potential and the distribution function of interparticle distances. However, these relationships are not applicable to flocculated systems.

SUMMARY

This study has characterized the role of the steric length of a surfactant on the rheological response of a model nanopowder. Interaction energy calculations predict the depth of the attractive well for each surfactant, and the nanopowder exhibited a transition from a strongly flocculated system with constant elastic properties at very low

volume fraction to a nearly dispersed system. The structure of the flocculated systems was modeled from the rheological response, but the values were mixed. The limit of linearity tests were in accord with theoretical predictions of the fractal dimension, but the scaling of elastic modulus did not produce fractal dimensions that agree with theory. Also, the dispersed system did not exhibit data trends in accord with conventional rheological models. The predicted maximum in solids loading is lower than would be expected from strict geometrical space filling considerations, and an additional attractive interaction is postulated for the system. This interaction could be attributed to dissolved gases in the system forming bubbles at the particle contact points. Future studies recommended to understand the behavior of these systems include contact angle measurements of the acids on alumina surfaces to ensure that wetting is good and characterize gas bubble hypothesis, as well as atomic force microscopy of adhesion measurements. The fractal dimension of the systems should also be characterized using either light scattering or neutron scattering studies.

REFERENCES

1. N.S. Bell, "Dispersion Properties of an Alumina Nanopowder using Molecular, Polyelectrolyte, and Steric Stabilization," accepted *J. Nanoscience and Nanotechnology*, (2003).
2. W.B. Russel, "Review of the Role of Colloidal Forces in the Rheology of Suspensions," *J. Rheol.* **24** (1980) 287-317.
3. W.B. Russel, "Concentrated Colloidal Dispersions," *MRS Bulletin* **16** [8] (1991) 27-30.
4. R.L. Hoffman, "Interrelationships of Particle Structure and Flow in Concentrated Suspensions," *MRS Bulletin* **16** [8] (1991) 32-37.
5. L. Bergstrom, "Sedimentation of Flocculated Alumina Suspensions: γ-Ray Measurements and Comparison with Model Predictions," *J. Chem. Soc. Faraday Trans.*, **88** (1992) pp. 3201-3211.
6. L. Bergstrom, C.H. Schilling, and I.A. Aksay, "Consolidation Behavior of Flocculated Alumina Suspensions," *J. Am. Ceram. Soc.*, **75** (1992) pp. 3305-3314.
7. C.J. Rueb and C.F. Zukoski, " ," *J. Rheol.* , **41** (1997) p. 197.
8. J. A. Yanez, E. Laarz, and L. Bergstrom, "Viscoelastic Properties of Particle Gels," *J. Coll. Interf. Sci.*, **209** (1999) pp. 162-172.
9. M.C. Grant and W.B. Russel, "Volume Fraction Dependence of Elastic Moduli and Transition Temperatures for Colloidal Silica Gels," *Phys. Rev. E*, **47** (1993) 2606-2614.
10. J. W. Jansen, C.G. de Kruif, and A. Vrij, "Attractions in Sterically Stabilized Silica Dispersions I. Theory of Phase Separation," *J. Coll. Interface Sci.* **114** (1986) 471-480.
11. J. W. Jansen, C.G. de Kruif, and A. Vrij, "Attractions in Sterically Stabilized Silica Dispersions II. Experiments on Phase Separation Induced by Temperature Variation," *J. Coll. Interface Sci.* **114** (1986) 481-4910.
12. J. W. Jansen, C.G. de Kruif, and A. Vrij, "Attractions in Sterically Stabilized Silica Dispersions III. Second Virial Coefficient as a Function of Temperature, as Measured by Means of Turbidity," *J. Coll. Interface Sci.* **114** (1986) 492-500.
13. J. W. Jansen, C.G. de Kruif, and A. Vrij, "Attractions in Sterically Stabilized Silica Dispersions, IV. Sedimentation" *J. Coll. Interface Sci.* **114** (1986) 501-504.
14. J.A. Horn and B.R. Patterson, "Thermally Induced Reversible Coagulation in Ceramic Powder-Polymer Liquid Suspensions," *J. Am. Ceram. Soc.* **80** (1997) 1789-1797.
15. M. Colic, G.V. Franks, M. L. Fisher, and F.F. Lange, "Effect of Counterion Size on Short Range Repulsive Forces at High Ionic Strengths," *Langmuir*, **13**, (1997) 3129-3135.
16. G.V. Franks, M. Colic, M.L. Fisher, and F.F. Lange, "Plastic-to-Brittle Transition of Consolidated Bodies: Effect of Counterion Size," *J. Coll. Interf. Sci.*, **193** (1997) 96-103.
17. C. Friedrich and H. Braun, "Generalized Cole-Cole Behavior and its Rheological Relevance," *Rheol. Acta*,**31** (1992) 309-322.
18. A. Zupancic, R. Lapasin, and A. Kristoffersson, "Influence of Particle Concentration on Rheological Properties of Aqueous α-Al_2O_3 Suspensions," *J. Eur. Ceram. Soc.*, **18** (1998) 467-477.
19. W.H. Shih, W.Y. Shih, S.-I. Kim, J. Liu, I.A. Aksay, " Scaling Behavior of the Elastic Properties of Colloidal Gels,"*Phys. Rev. A* **42** (1990) 4772-4779.
20. P. Meakin, "Simple Models for Particle Aggregation, Deposition, and Segregation," *Mat. Res. Soc. Symp. Proc.* **180** (1990) 141-152.
21. P. Meakin, "Diffusion-Limited Aggregation in Three Dimensions: Results from a New Cluster-Cluster Aggregation Model," *J. Colloid Interface Sci.*, **102** (1984) 491-504.

22. P. Meakin, "Formation of Fractal Clusters and Networks by Irreversible Diffusion Limited Aggregation," *Phys. Rev. Lett.*, **51**(1983) 1119-1122.
23. M.Y. Lin, H.M. Lindsay, D.A. Weitz, R. Ball, R. Klein, P. Meakin, "Universal Reaction Limited Colloid Aggregation,"*Phys. Rev A* **41** (1990) 2005.
24. J. Liu, W.Y. Shih, M.Sarikaya, and I.A. Aksay, "Fractal Colloidal Aggregates with Finite Interparticle Interactions: Energy Dependence of the Fractal Dimension," *Phys. Rev. A*, **41** (1990) 3206-3213.
25. W.Y. Shih, I.A. Aksay, R. Kikuchi, "Reversible Growth Model: Cluster-Cluster Aggregation with Finite Binding Energies," *Phys. Rev. A*, **36** (1987) 5015-5019.
26. E. Dickenson, "Structure and Rheology of Simulated Gels Formed from Aggregated Colloidal Particles," *J. Coll. Interface Sci.* **225** (2000) 2-15. .
27. D. Stauffer and A. Aharony, Introduction to Percolation Theory, Taylor and Francis, Philiadelphia, PA, 1991.
28. C. Allain, M. Clortre, and M Wafra, "Aggregation and Sedimentation in Colloidal Suspensions," *Phys. Rev. Lett.,* **74** (1995) 1478-1481.
29. R. Buscall, P.D. Mills, J.W. Goodwin, and D.W. Lawson, *J. Chem. Soc. Faraday Trans 1*. **84** (1988) 4249.
30. A.L. Ogden, and J. A. Lewis, "Effect of Nonadsorbed Polymer on the Stability of Weakly Flocculated Suspensions," *Langmuir*, **12** (1996) pp. 3413-3424.
31. J. Vermant, L. Raynaud, J. Mewis, B. Ernst, and G.G. Fuller, "Large-Scale Bundle Ordering in Sterically Stabilized Latices," *J. Coll. Interface Sci.* **211** (1999) 221-229.
32. N. Ishida, M. Sakamoto, M. Miyahara, and K. Higashitani, "Optical Observation of Gas Bridging between Hydrophobic Surfaces in Water," *J. Colloid Interface Sci.* **253,** (2002) 112–116.
33. N. Ishida, M. Sakamoto, M. Miyahara, and K. Higashitani, "Attraction between Hydrophobic Surfaces with and without Gas Phase," *Langmuir* **16**, (2000) 5681-5687.
34. L. Marshall and C.F. Zukoski, "Experimental Studies on the Rheology of Hard-Sphere Suspensions near the Glass Transition," *J. Phys. Chem.* **94** (1990) 1164-1171.
35. L. Raynaud, B. Ernst, C. Verge, and J. Mewis, "Rheology of Aqueous Latices with Adsorbed Stabilizer Layers," *J. Coll. Interface Sci.I* **181** (1996) 11-19.
36. J. Mewis and J. Vermant, "Rheology of Sterically Stabilized Dispersions and Latices," *Prog. Org. Coatings* **40** (2000) 111-117. J. Vermant, L. Raynaud, J. Mewis, B. Ernst, and G.G. Fuller, "Large-Scale Bundle Ordering in Sterically Stabilized Latices," *J. Coll. Interface Sci.* **211** (1999) 221-229.
37. I.M. Krieger and T.J. Doughtery, *Trans. Soc. Rheol.* **111** (1959) 137.
38. D. Quemada, Advances in Rheology, Universidad Nacionai Autonama de Mexico: 1984, Vol. 2.

DISTRIBUTION

3	Sandia National Laboratories	MS 1411	N.S. Bell 1846
1			J. Liu 1846
1			M. Rodriguez 1822
1			D. Tallent 1822
1		1310	R.P. Goehner
1		9018	Central Technical Files 8945-1
2		0899	Technical Library, 9616